Variants in the SOX9 transactivation middle domain induce axial skeleton dysplasia and scoliosis

Lianlei Wang[1,2,3#], Zhaoyang Liu[4#*], Sen Zhao[1,3#], Kexin Xu[1,3,6#], Valeria Aceves[5], Cheng Qiu[2], Benjamin Troutwine[5], Lian Liu[1,3], Samuel Ma [5], Yuchen Niu[3,6,7], Shengru Wang[1,3,6], Suomao Yuan[2], Xiaoxin Li[3,6,7], Lina Zhao[3,6,7], Xinyu Liu[2], Zhihong Wu[3,6,7], Terry Jianguo Zhang[1,3,6*], Ryan S. Gray[5*], and Nan Wu[1,3,6*]

1. Department of Orthopedic Surgery, State Key Laboratory of Complex Severe and Rare Diseases, Peking Union Medical College Hospital, Peking Union Medical College, and Chinese Academy of Medical Sciences, Beijing, China.
2. Department of Orthopedic Surgery, Qilu Hospital of Shandong University, Jinan, Shandong, China.
3. Beijing Key Laboratory for Genetic Research of Skeletal Deformity, Beijing, China.
4. Center for Craniofacial Molecular Biology, Herman Ostrow School of Dentistry, University of Southern California, Los Angeles, CA, USA; Department of Nutritional Sciences, Dell Pediatric Research Institute, University of Texas at Austin, Austin, TX, USA.
5. Department of Nutritional Sciences, Dell Pediatric Research Institute, The University of Texas at Austin, Dell Medical School, Austin, TX, USA.
6. Key laboratory of big data for spinal deformities, Chinese Academy of Medical Sciences, Beijing, China.
7. Medical Research Center, Peking Union Medical College Hospital, Peking Union Medical College, and Chinese Academy of Medical Sciences, Beijing, China.

# These authors contributed equally to this work.

***Authors for correspondence**

Nan Wu

No. 1 Shuaifuyuan, Beijing 100730, China

Phone: 86-10-69151108, dr.wunan@pumch.cn

Ryan S. Gray

1400 Barbara Jordan Blvd., Austin, TX 78723, USA

Phone: 512-495-5052, ryan.gray@austin.utexas.edu

Terry Jianguo Zhang

No. 1 Shuaifuyuan, Beijing 100730, China

Phone: 86-10-69151108, jgzhang_pumch@yahoo.com

Zhaoyang Liu

2250 Alcazar Street, Los Angeles, CA 90033, USA

Phone: 323-442-2549, liuzhaoy@usc.edu

Conflicts of interest

The authors have declared that no conflict of interest exists.

ABSTRACT

SOX9 is an essential transcriptional regulator of cartilage development and homeostasis. In humans, dysregulation of *SOX9* is associated with a wide spectrum of skeletal disorders, including campomelic and acampomelic dysplasia, and scoliosis. The mechanism of how *SOX9* variants contribute to the spectrum of axial skeletal disorders is not well understood. Here, we report four novel pathogenic variants of *SOX9* identified in a large cohort of patients with congenital vertebral malformations. Three of these heterozygous variants are in the HMG and DIM domains, and for the first time, we report a pathogenic variant within the transactivation middle (TAM) domain of *SOX9*. Probands with these variants exhibit variable skeletal dysplasia, ranging from isolated vertebral malformation to acampomelic dysplasia. We also generated a *Sox9* hypomorphic mutant mouse model bearing a microdeletion within the TAM domain ($Sox9^{Asp272del}$). We demonstrated that disturbance of the TAM domain with missense mutation or microdeletion results in reduced protein stability but does not affect the transcriptional activity of SOX9. Homozygous $Sox9^{Asp272del}$ mice exhibited axial skeletal dysplasia including kinked tails, ribcage anomalies, and scoliosis, recapitulating phenotypes observed in human, while heterozygous mutants display a milder phenotype. Analysis of primary chondrocytes and the intervertebral discs in $Sox9^{Asp272del}$ mutant mice revealed dysregulation of a panel of genes with major contributions of the extracellular matrix, angiogenesis, and ossification-related processes. In summary, our work identified the first pathologic variant of *SOX9* within the TAM domain and demonstrated that this variant is associated with reduced SOX9 protein stability. Our finding suggests that reduced SOX9 stability caused by variants in the TAM domain may be responsible for the milder forms of axial skeleton dysplasia in humans.

69 **Keywords**: *SOX9* (*SRY-Box 9*), Campomelic Dysplasia, Skeletal Dysplasia, Congenital

70 Vertebral Malformations, Scoliosis, Protein Stability

71

INTRODUCTION

SRY-Box 9 (*SOX9*) encodes a transcriptional regulator essential for the development and homeostasis of cartilaginous tissues (1). SOX9 is required to secure the commitment of skeletogenic progenitor cells to the chondrocyte lineage and direct the formation of multiple elements of the axial and appendicular skeleton (2). Ablation of *Sox9* in mesenchymal progenitors of the limb bud or during the early stages of chondrogenesis results in a complete failure of cartilage and bone generation or severe chondrodysplasia (3). SOX9 is also required for axial skeletogenesis. Deletion of *Sox9* in the notochord prevents the formation of its cartilage-rich perinotochordal sheath and results in notochordal cell death (4). Conditional inactivation of *Sox9* in the *Scx*+/*Sox9*+ cell populations cause severe hypoplasia of the ribcage and sternum and defective formation of the vertebral bodies and intervertebral discs of the spine (5). Recent studies also demonstrate that *SOX9* plays a crucial role in maintaining the homeostasis of postnatal intervertebral discs (6, 7). These studies affirm that *SOX9* is critical in vertebral column development and maintenance.

SOX9 is featured with a highly conserved SRY-related high-mobility-group-box (HMGbox) DNA-binding domain, which is found in all SOX family proteins that act as transcriptional regulators in cell fate determination and differentiation in a variety of lineages (2, 8). Two molecules of SOX9 can form homodimer via the self-dimerization domain (DIM) upon binding in the minor groove of a DNA sequence composed of two SOX recognition motifs, oriented head-to-head and separated by 3-4 nucleotides (9). In addition to the N-terminal HMG and DIM domains, SOX9 is also composed of three additional domains: the transactivation domain in the middle of the protein (TAM), the transactivation domain at the C-terminal (TAC), and the PQA (Proline, Glutamine, and Alanine-rich) domain (8). In vitro analyses show that TAM and TAC domains can work independently and synergistically to control the

transactivation of SOX9 (8). PQA domain has no major role in SOX9 transactivation but may help mediate SOX9 activity in specific contexts (8, 10). The molecular functions of these C-terminal domains are proposed to provide synergistic binding of transcriptional co-activators and basal transcriptional machinery (8). For instance, the CREB (cAMP response element-binding protein) transcription factor can be co-immunoprecipitated using the C-terminal transactivation domains but not with the N-terminal domains of SOX9 (11).

Variants in *SOX9* are associated with a range of skeletal deformities including campomelic dysplasia (CMPD, OMIM 114290), acampomelic dysplasia (acampomelic CMPD), and scoliosis (1, 12-15). Heterozygous point mutations (missense, nonsense, frameshift, and splice site) in *SOX9* cause CMPD, characterized by congenital shortening and bending of long bones, vertebral malformation, rib anomalies, dysplasia of scapula, and dysmorphic facial features (14, 16-22). Heterozygous *Sox9* knockout mice phenocopy most of the skeletal abnormalities of this syndrome (23). Though it is generally believed that haploinsufficiency for *SOX9* can underlie CMPD, a recent study implicates that combined haploinsufficiency/hypomorphic and dominant-negative mechanisms can apply for some *SOX9* CMPD mutations in a target gene and cell context-dependent manner (24). Roughly 10% of CMPD patients who do not display bending of long bones are subclassified as acampomelic CMPD (25, 26). Many of the *SOX9* variants causing CMPD are located in DIM and HMG domains, which are essential for the dimerization and DNA binding properties of the SOX9 protein (19, 27) and SOX9-dependent regulation of genes such as *Col2a1* (28, 29) and *Col11a2* (30). These patients usually exhibit severe skeletal abnormalities, including deformities of the long tubular bones, and some of them may present with sex reversal. CMPD can also arise from variants in the TAC and PQA domains of SOX9 (31, 32). Frameshift and nonsense mutations reported in these domains usually result in a truncated SOX9 protein and severe CMPD and sex reversal (32, 33). On the other hand, patients with acampomelic CMPD are more likely to have missense variants, genomic

rearrangement with breakpoints upstream of *SOX9*, or a *SOX9* upstream deletion (34). We have previously identified a recurrent missense variant at the prolines/glutamines/serines (PQS) domain (now called TAC domain) of *SOX9* in patients with congenital vertebral malformations but without other systematic deformities (35), which is one of the first non-truncating variants reported in the TAC domain that is associated with a milder form of axial skeleton dysplasia. No missense or nonsense variant in the TAM (previously called K2) domain has been reported so far (36, 37). These observations suggest that locations of variants in different domains of SOX9 might underline a spectrum of skeletal dysplasia from CMPD to milder forms that primarily or exclusively affect the axial skeleton.

To this end, we investigated ultra-rare SOX9 variants within a large cohort of congenital vertebral malformations and identified four novel variants of *SOX9*. We report the first pathologic missense variant of *SOX9* within the TAM domain associated with a milder form of axial skeletal dysplasia and demonstrated that variants in the TAM domains result in reduced SOX9 protein stability. We also generated a *Sox9* hypomorphic mouse model with in-frame microdeletion in the TAM domain which recapitulates some of the skeletal phenotypes observed in the human patient. This work enhances our understanding of SOX9 function in the axial skeleton and provides new insights into the roles of different *SOX9* domains in the spectrum of skeletal dysplasia.

RESULTS

Rare and *de novo SOX9* variants identified in individuals with various severity of skeletal dysplasia

We investigated ultra-rare *SOX9* variants with a cohort of 424 patients of congenital vertebral malformations, which consists of a broad spectrum of syndromic and non-syndromic vertebral deformities. Four novel heterozygous missense variants were identified from four probands, including three *de novo* variants (c.218T>C, p.Ile73Thr; c.337A>C, p.Met113Leu and c.826G>T, p.Gly276Cys) and one variant (c.398C>G, p.Ala133Gly) with unknown inheritance (Figure 1, A and B, and Table 1). The clinical and genetic features of these probands are summarized in Table 1. No pathogenic variants in other genes were identified. Family history assessments of the probands show that their parents and siblings are all uneventful.

Two of the four probands RDD2003P0397 (Figure 1B) and SCO2003P0412 (Figure 1C) exhibited deformities consistent with the clinical manifestations of acampomelic CMPD. RDD2003P0397 presented congenital vertebral malformation caused by the fusion of the cervical vertebra (Figure 1B). Exome sequencing identified a *de novo* heterozygous missense variant c.337A>C (p.Met113Leu) located within the HMG-box of *SOX9* (Figure 1A). Two missense variants (Met113Thr and Met113Val) that affect the same amino acid have been reported previously in a CMPD patient (Met113Thr) and an acampomelic CMPD patient (Met113Val), respectively (38, 39). SCO2003P0412 presented congenital kyphosis (Figure 1C). He had a heterozygous missense variant (c.398C>G, p.Ala133Gly) within the HMG-box of *SOX9* with an unknown inheritance origin (Figure 1C). No pathogenic variant of this amino acid has been reported previously. Notably, Ala133Gly is predicted to be highly deleterious (combined annotation dependent depletion [CADD] score = 24.1).

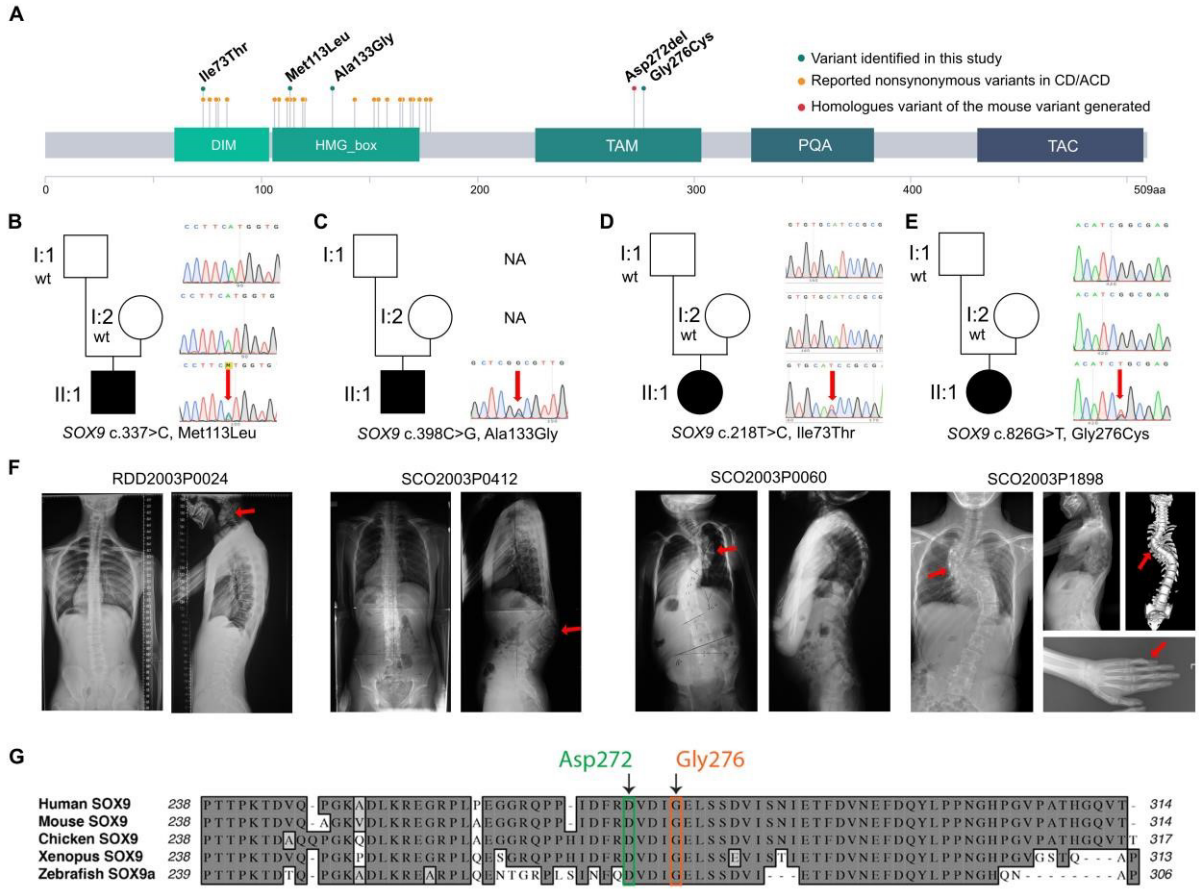

Figure 1. Identification of *de novo* or sporadic *SOX9* variants in four individuals with skeletal dysplasia. (**A**) A schematic presentation of the SOX9 protein. *SOX9* variants identified in this study (green dots), previous studies (orange dots), and the homologs of the mouse variant generated in this study (the red dot) are labeled. (**B-E**) Sanger sequencing results of *de novo SOX9* variants in three trio families and one sporadic case. (**F**) Clinical presentation of the four individuals carrying the *SOX9* variants. Red arrows indicate skeletal malformations. G. Both the Asp272 and Gly276 variants are highly conserved residues. *CMPD: Campomelic Dysplasia; acampomelic CMPD: Acampomelic Dysplasia; DIM: dimerization domain; HMG: high mobility group domain; TAM: transactivation middle, PQA: proline, glutamine, and alanine-rich domain; TAC: transactivation C-terminal.*

In contrast to these two cases diagnosed as acampomelic CMPD, the third proband SCO2003P0060 presented a milder skeletal dysplasia phenotype characterized by a wedged vertebra at T6 and thoracic scoliosis (Figure 1D). She also presented with short stature and kyphoscoliosis (Table 1). She carried a *de novo* variant c.218T>C (Ile73Thr) located in the

DIM domain of *SOX9* (Figure 1A). A variant affecting the same amino acid (Ile73Asn) has been reported previously in a patient with multiple congenital anomalies (40). This c.218T>C (Ile73Thr) variant has not been included in the gnomAD (v2.1.1, https://gnomad.broadinstitute.org, accessed on January 5, 2023), and it is classified as likely pathogenic (PM2_Supporting + PS3_Supporting + PS2 + PM5_Supporting) according to the ACMG guideline (41).

In the fourth proband (SCO2003P1898), we identified a *de novo* variant c.826G>T (Gly276Cys) located at the TAM domain (8) of *SOX9* (Figure 1A). This Gly276 residual is highly conserved among vertebrate orthologues (Figure 1G). To our knowledge, this is the first missense mutation reported within the TAM domain in humans. This proband exhibited fused vertebrae from T6-T11 and spinal bifida occulta of L4-L5 (Figure 1E). She also exhibited thoracic scoliosis and clinodactyly of the distal 5th phalange (Figure 1E). Interestingly, the multiple fusion of thoracic vertebrae phenotype in this proband was distinct from the other three patients and the classical CMPD/ acampomelic CMPD patients, suggesting that variants in the TAM domain of *SOX9* may be associated with a distinct type of skeletal anomalies.

To further characterize the impact of *SOX9* variants, we modeled the potential structural effects of these mutations predicted by Alpha Fold (Supplemental Figure 1, https://alphafold.ebi.ac.uk) (42). The evolutionally conserved *SOX9* Ile73, Met113, and Ala133 residues are predicted to help stabilize alpha-helical regions (Supplemental Figure 1, B-D) within the regions with high confidence of prediction or within areas where structural information was empirically determined (unpublished PDB data: 4EUW and 4S2Q). The highly conserved *SOX9* Gly276 residue (Fig. 1G) is predicted to hydrogen bond interact with Asp274 (Supplemental Figure 1E) in a putative helical region of the protein. Altogether, the *in silico* evidence showed that the affected residues are highly conserved among vertebrate orthologues, and alteration of these residues may lead to compromised protein structure and

203 altered interactions with other residues, which may jeopardize the function and structural
204 stability of the SOX9 protein.

205 **Effects of the *SOX9* variants on DNA-binding and transcriptional activities of SOX9**

206 Next, we sought to understand how *SOX9* variants affect the DNA-binding and transcriptional
207 activities of the SOX9 protein using electrophoretic mobility shift assay (EMSA) and luciferase
208 reporter assay. We synthesized two sets of EMSA probes derived from the enhancer region of
209 the mouse *Col11a2* gene (30). Each probe contains a canonical SOX9 DNA-binding motif and
210 was named *Col11a2* B/C and *Col11a2* D/E respectively. An equal amount of SOX9 wild-type
211 and variants proteins were incubated with these probe sets for EMSA analyses (Supplemental
212 Figure 2). We discovered that both *SOX9* variants within the HMG-box (Met113Leu and
213 Ala133Gly) display impaired DNA-binding

220

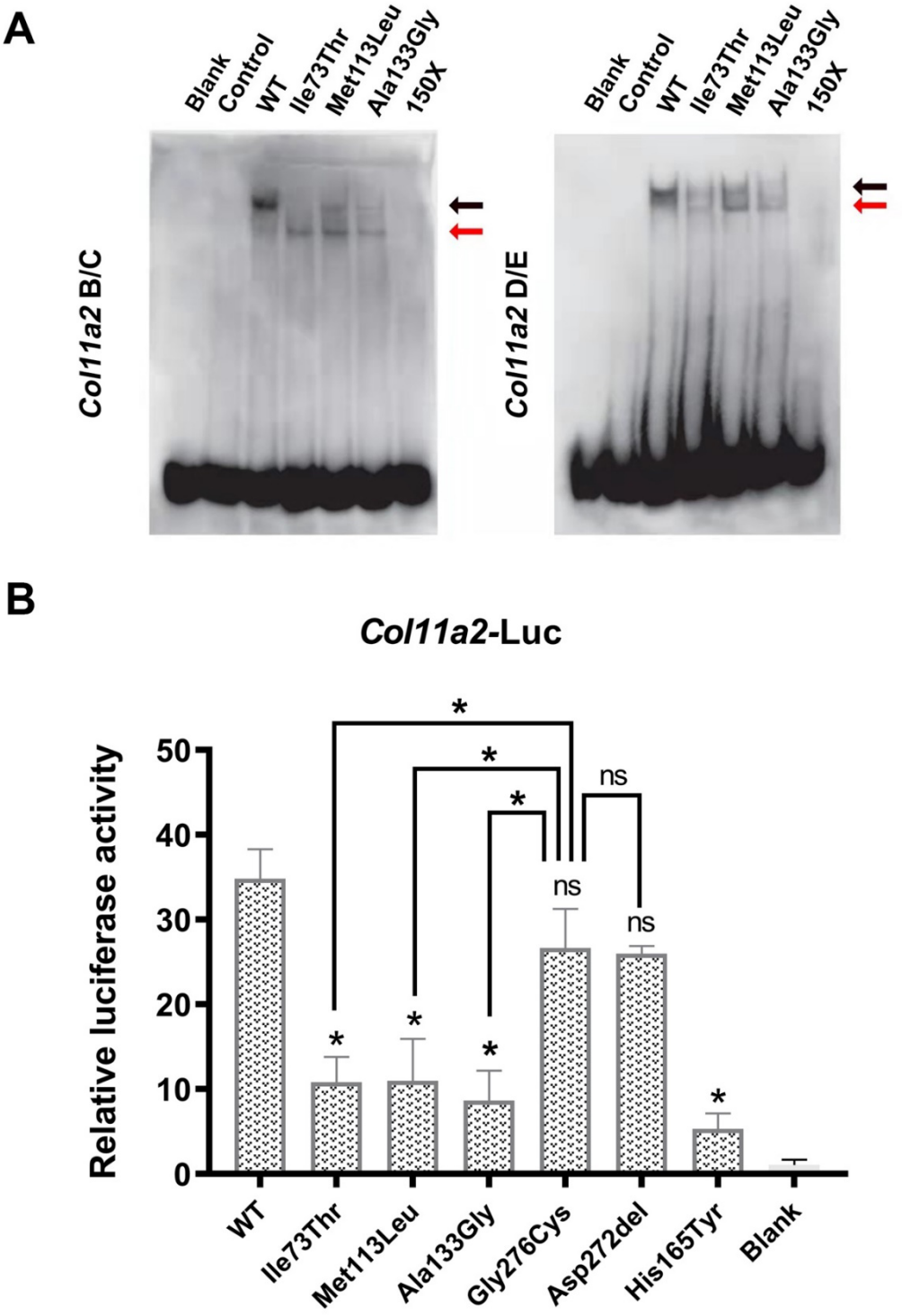

Figure 2. Effects of the *SOX9* variants on DNA-binding and transcriptional activities of SOX9. (A) Electrophoretic mobility shift assay (EMSA) was performed on the whole cell lysate extracted from Cos-7 cells. Cell lysate with no transfection was used as a blank control (Blank). Cos-7 cells transfected with a GFP control construct were used as a mock control (Control). The 150-fold unlabeled DNA probes (150X) were incubated with cell lysate of Cos-7 cells transfected with wild-type SOX9 protein. Free probes were detected at the bottom of the gel.

The bound dimer and monomer SOX9 proteins are indicated with black and red arrows, respectively. **(B)** Luciferase assay was performed on wild-type (WT) SOX9 protein and various SOX9 variant mutant proteins using a *Col11a2*-Luc construct. His165Tyr variant protein was used as a negative control (31). *The statistical difference is evaluated by one-way ANOVA followed by Tukey's multiple comparison test. The data are the mean of n = 3 independent experiments. Error bars show one standard deviation. * p<0.05 ** p<0.01 ns: not significant.*

capability characterized by decreased probe binding signal (Figure 2A, black arrows). The *SOX9* variant within the DIM domain (Ile73Thr), which is an essential domain for the dimerization of SOX9 proteins (43), showed reduced DNA-binding capability and loss of dimerization (Figure 2A, black arrows, and red arrows). To define if these variants affected SOX9-dependent gene transcription, we co-transfected various SOX9-expression vectors with a luciferase reporter construct (named *Col11a2*-Luc) which contains 4 tandem copies of the canonical SOX9 DNA-binding motif *Col11*a2 D/E (Supplemental Figure 3 and Supplemental Table 2) (30, 44). We showed that both the HMG-box variants (Met113Leu and Ala133Gly) and the DIM domain variant (Ile73Thr) exhibited decreased transcriptional activity of SOX9 (Figure 2B). In contrast, the variant in the TAM domain (Gly276Cys) did not obviously compromise the transcriptional activity of SOX9 compared with the wild-type protein but showed significantly higher transcriptional activity compared with the Ile73Thr, Met113Leu, and Ala133Gly variants (Figure 2B). Taken together, these data suggest that the variants in HMG and DIM domains are likely affecting the DNA-binding capabilities and homotypic interactions of SOX9, which may lead to compromised SOX9-dependent transcriptional activities. In contrast, variants in the TAM domain may still allow for some transcriptional activity at the canonical SOX9 targets thus permitting partial SOX9-dependent function.

A TAM domain mutation in mice leads to dose-dependent reductions of SOX9 expression and tail kinking during perinatal development

To further our understanding of the role of the TAM domain variant in skeletal dysplasia, we set out to use a CRISPR-Cas9 gene-editing approach to knock in the human variant Gly276Cys in the mouse (Figure 1E). After multiple injections, we isolated only three CRISPR-injected mice as adults (0.3%; n=123 implanted), likely due to haploinsufficient lethality of *Sox9* in the mouse (23). Serendipitously, we obtained an in-frame microdeletion allele ($Sox9^{em1Rgray}$), which deleted Asp272 (Asp272del), four amino acids upstream of Gly276Cys within the TAM domain (Figure 1A, Figure 3, A and N). Like the Gly276 residual, the Asp272 residual is also highly conserved among vertebrate orthologues (Figure 1G) and is predicted to hydrogen bond interact with Asp274 by Alpha Fold structural prediction (Supplemental Figure 1E). Intercross of these $Sox9^{Asp272del/+}$ mice (hereafter called $Sox9^{del}$) generated $Sox9^{del/del}$ mutant mice at Mendelian ratios that are indistinguishable from the $Sox9^{del/+}$ or wild-type ($Sox9^{+/+}$) littermates at birth. However, by postnatal (P) day 5 $Sox9^{del/del}$ mutant mice exhibited a fully penetrant kinked tail phenotype (100%, n=12) (Figure 3D, red arrow). In contrast, heterozygous $Sox9^{del/+}$ and wild-type littermates uniformly displayed normal tails (Figure 3, B and C).

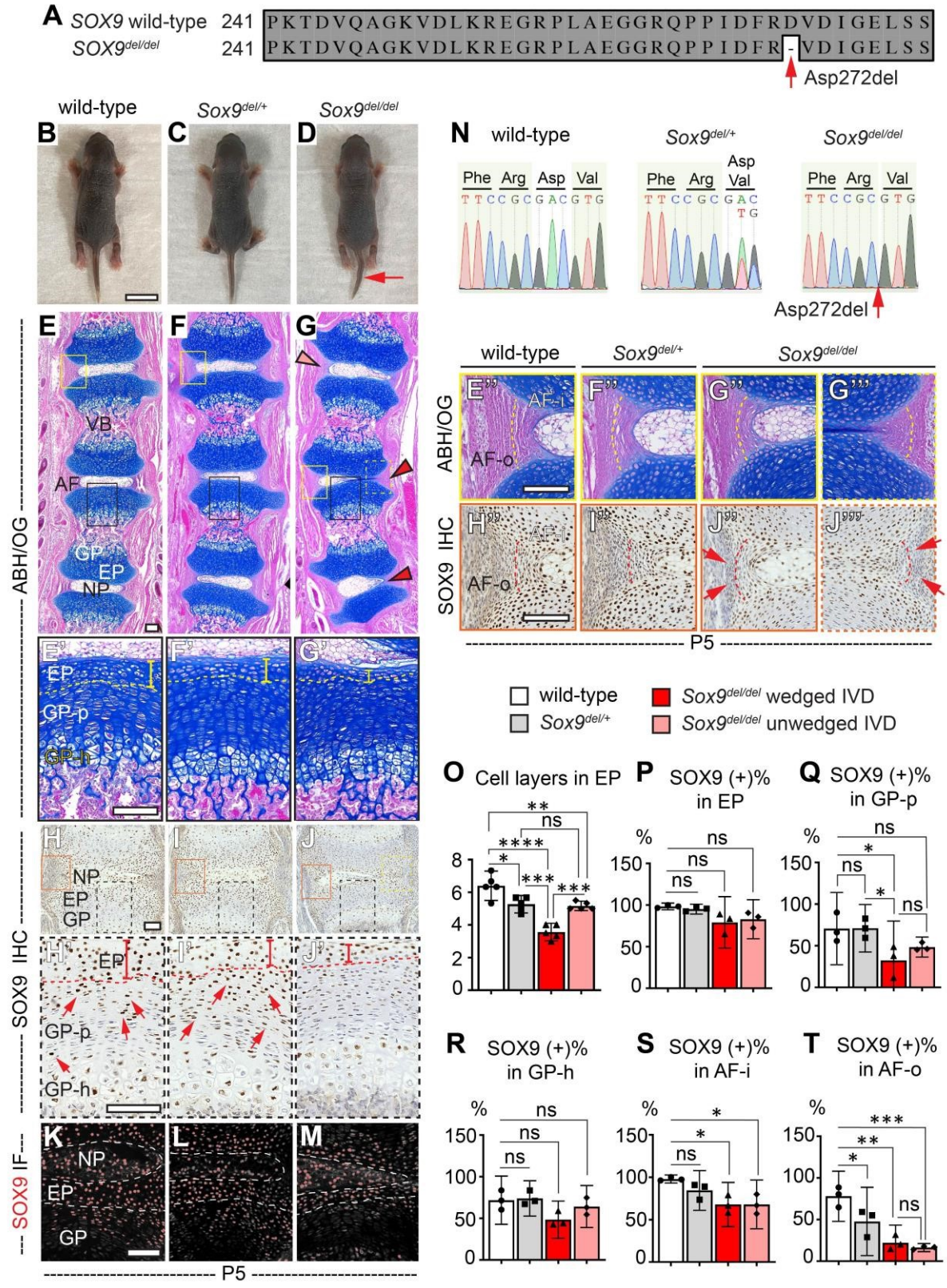

Figure 3. A TAM domain mutation in mice leads to dose-dependent reductions of SOX9 expression and tail kinking during perinatal development. (**A**) Illustration of the in-frame deletion of Asp272 in the *Sox9*$^{del/del}$ mutant mouse. The red arrow indicates the Asp272del mutation. (**B-D**) At P5, an obvious kinked tail phenotype was observed in 100% of the *Sox9*$^{del/del}$ mutant mice, but not in heterozygous *Sox9*$^{del/+}$ or wild-type littermates.

(n=12 for *Sox9*$^{del/del}$ mice, n=8 for *Sox9*$^{del/+}$ and wild-type littermates). (**E-G'''**) Alcian Blue Hematoxylin /Orange G (ABH/OG) staining performed on P5 mouse tail sections revealed normal segmentation of the vertebral bodies and typical proteoglycan staining of IVD and growth plate in *Sox9*$^{del/del}$ mutant mice (**G**) compared with the wildtype (**E**) and *Sox9*$^{del/+}$ (**F**) littermates. Red and pink arrowheads indicate wedged and unwedged IVDs in *Sox9*$^{del/del}$ mutant mouse, respectively. Higher magnification images of the endplate and growth plate and the annulus fibrosus are shown in (**E'-G'**) and (**E''-G'''**). The endplate is indicated with a dotted line and a vertical bar in (**E'G'**). The boundary between inner and outer annulus fibrosus is indicated with a dotted line in (**E''-G'''**). (n=4 for each genotype). (**H-J''**) Immunohistochemistry (IHC) analyses of SOX9 performed on P5 mouse tail sections. Higher magnification images of the endplate and growth plate and the annulus fibrosus are shown in (**H'-J'**) and (**H''-J'''**). The endplate is indicated with a dotted line and a vertical bar in (**H'-J'**). SOX9 expression in proliferative growth plates is indicated with red arrows in (**H'**) and (**I'**). The boundary between inner and outer annulus fibrosus is indicted with a dot-line in (**H''-J'''**). The absence of SOX9 expression in the outer annulus fibrosus is indicated with red arrows in (**J''**) and (**J'''**). (n=4 for each genotype.) (**K-M**) Immunofluorescence (IF) analyses of SOX9 were performed on P5 mouse tail sections. (n=6 for each genotype.) (**N**) Sanger sequencing results of wild-type, *Sox9*$^{del/+,}$ and *Sox9*$^{del/del}$ mice. The red arrow indicates the Asp272del mutation. (**O-T**) Quantification of the number of cell layers in endplate (**O**), and quantification of the percentile of SOX9 (+) cells in endplate (**P**), proliferative growth plate (**Q**), hypertrophic growth plate (**R**), inner annulus fibrosus (**S**), and outer annulus fibrosus (**T**) in three genotypes of mice. Bars are plotted with mean and 95%CI. Each dot represents one mouse analyzed. The statistical difference is evaluated by one-way ANOVA followed by Tukey's multiple comparison test. * $p<0.05$, **: $p<0.01$, ***$p<0.001$. ns: not significant. For (**O**), n=5 for each genotype; for (**PT**), n=3 for each genotype. *Scale bars: 10mm in **B**; 100μm in **E-E'''**, **H-H'''** and **K**. VB: vertebral body; AF: annulus fibrosus; EP: endplate; GP: growth plate; NP: nucleus pulposus; GP-p: proliferative growth plate; GPh: hypertrophic growth plate; AF-i: inner annulus fibrosus; AF-o: outer annulus fibrosus.*

Many congenital vertebral malformations are due to patterning defects of embryonic somites which contribute to the formation of vertebral bodies and intervertebral discs (IVDs) (45). Histological analysis of *Sox9*$^{del/del}$ mutant mouse tails at P5 revealed normal segmentation and ossification of the vertebral bodies and typical proteoglycan staining in the IVDs and growth plates (Figure 3, E-G). However, the *Sox9*$^{del/del}$ mice showed wedging of the IVDs in regions of tail kinking, a shift of the nucleus pulposus toward the convex side (Figure 3G, red arrowheads), and compression of annulus fibrosus on the concave side of the curvature (Figure 3G'''). In contrast, unwedged IVDs adjacent to severe curvatures could display comparably normal structures (Figure 3G, pink arrowhead, and Supplemental Figure 4A). Detailed analysis of the

293 tail sections revealed that the thickness of the cartilaginous endplate of the IVDs is reduced in
294 *Sox9*$^{del/+}$ and the *Sox9*$^{del/del}$ mutant mice compared with that of the wild-type mice (Figure 3, E'
295 and G', yellow bars) quantified by the number of cell layers within the endplate (Figure 3O).
296 The number of endplate cell layers in the unwedged IVDs of the *Sox9*$^{del/del}$ mutant mice is
297 slightly increased compared with that of the wedged IVDs but is still reduced in comparison
298 with the wild-type mice (Figure 3O and Supplemental Figure 4A').

299 We next sought to determine how SOX9 expression was affected in *Sox9*$^{del/del}$ mutant
300 tissues. Immunohistochemistry (IHC) and immunofluorescence (IF) analyses of P5 tail sections
301 revealed that SOX9 expression is regionally reduced in the *Sox9*$^{del/+}$ and the *Sox9*$^{del/del}$ mutant
302 mice (Figure 3, H-J' and K-M). We observed a decreased SOX9 expression in the proliferative
303 growth plate adjacent to the wedged IVDs but not the unwedged IVDs of the *Sox9*$^{del/del}$ mutant
304 mice (Figure 3, H'-J' and Q, and Supplemental Figure 4, B-B'). No difference in SOX9
305 expression was observed in the hypertrophic growth plate (Figure 3, H'-J' and R) nor the
306 endplate (Figure 3P) among the three genotypes. We also observed reduced expression of
307 SOX9 in both inner and outer layers of the annulus fibrosus of the *Sox9*$^{del/del}$ mutant mice in
308 both wedged and unwedged IVDs (Figure 3, H''-H''' and 3S-T, and Supplemental Figure
309 4B''), with more pronounced effects on the outer layers (Figure 3, J''-J''', red arrows; and
310 Figure 3T), as well as decreased *SOX9* expression in the outer annulus fibrous of the *Sox9*$^{del/+}$
311 mice (Figure 3T). IHC analyses of type II collagen (COLII) and type X collagen (COLX)
312 showed a comparable pattern of staining at this age among all three genotypes (Supplemental
313 Figure 4, C-H). All these results suggest that the mutation in the TAM domain leads to a dose-
314 dependent mild reduction of SOX9 expression in various compartments of the spinal tissues,
315 associated with a tail kinking phenotype during perinatal development. However, the overall
316 patterning and segmentation of the vertebral bodies are not affected.

Sox9^{Asp272del} is a hypomorphic loss-of-function allele

The tail kinking phenotype and the reduced SOX9 expression in the *Sox9*$^{del/+}$ and the *Sox9*$^{del/del}$ mutant mice are dose-dependent and region-specific, suggesting that the Asp272del microdeletion was behaving as a mild hypomorphic allele of *Sox9*. To test the nature of the *Sox9*^{del} allele, we assessed how skeletal development would be affected when the *Sox9*^{del} allele was *in trans* with an established floxed null allele of *Sox9* (*Sox9*^{flox}) (3). Previous studies show that completely inactivating *Sox9* in osteochondral progenitors using the *Col2a1-Cre* deleter strain (*Col2a1-Cre;Sox9*$^{flox/flox}$) resulted in embryonic lethality and severe chondrodysplasia in mutant embryos, while the heterozygous recombination of *Sox9* (*Col2a1-Cre;Sox9*$^{flox/+}$) caused perinatal lethality around P10 displaying dwarfism and kyphosis of the axial skeleton (3). Given these findings, we set out to assess skeletogenesis of the *Col2a1-Cre;Sox9*$^{flox/del}$ compound heterozygous mutants in comparison with the *Col2a1-Cre;Sox9*$^{flox/+}$ heterozygous mutants at P1.

The *Col2a1-Cre;Sox9*$^{flox/del}$ compound heterozygous mice were born at Mendelian ratio (n=8; total 67 pups) with a 63% survival rate at P1. Skeletal preparations showed increased defects of craniofacial and ribcage development and bending of the long bone in the *Col2a1-Cre;Sox9*$^{flox/del}$ compound heterozygous mutants compared with the *Col2a1-Cre;Sox9*$^{flox/+}$ heterozygous littermates (Supplemental Figure 5, B and C). To better quantify skeletal phenotypes, we analyzed the skull morphology with MicroCT imaging (Figure 4 and Supplemental Figure 5, D-F). We observed decreased skull size in *Col2a1-Cre;Sox9*$^{flox/del}$ compound heterozygous mutants (Figure 4, C-D) compared with Cre (-) controls (Figure 4, A and A') and *Col2a1-Cre;Sox9*$^{flox/+}$ heterozygous mutants (Figure 4, B and B'). However, we observed no significant change in the percentage of bone volume when normalized to total tissue volume (BV/TV) (Figure 4E), which is consistent with the previous report that *Sox9* deletion does not obviously affect osteoblast differentiation (3). Taken together, these genetic

342 studies provide functional evidence that the *Sox9*^{del} allele, which disturbs the TAM domain of

343 *SOX9*, is acting as a mild hypomorphic allele.

344

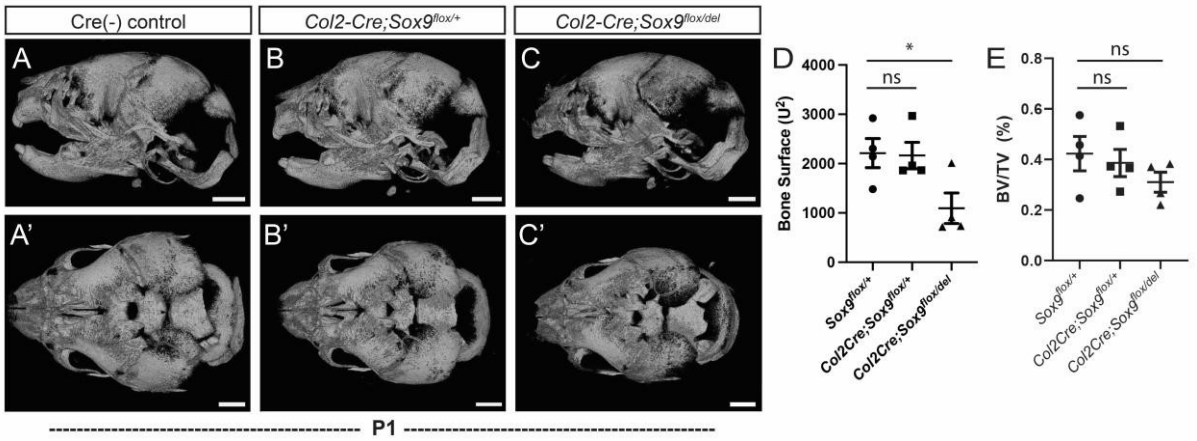

345

346 **Figure 4. *Sox9*^{Asp272del} is a hypomorphic loss-of-function allele.** (**A-C'**), 3D MicroCT renderings of mouse skulls
347 from Cre(-) control (**A, A'**), *Col2a1-Cre;Sox9*$^{flox/+}$ (**B, B'**), and *Col2a1-Cre;Sox9*$^{flox/del}$ mutant (**C, C'**) mice at P1
348 in lateral (**A-C**) or dorsal views (**A'-C'**). (**D**) Quantification of bone surface area (μm^2) of the skull shows a
349 reduced skull size of the *Col2a1-Cre;Sox9*$^{flox/del}$ compound heterozygous mutant mice (p= 0.0428) compared to
350 wild-type Cre(-) control mice. (**E**) Quantification of the percentage of bone volume vs tissue volume (BV/TV)
351 shows no loss of bone mass density in the skulls of *Col2a1-Cre;Sox9*$^{flox/del}$ mutant mice (p=0.2972) compared to
352 wild-type Cre(-) control mice. Bars are plotted with mean and standard deviation. Each dot represents one mouse
353 analyzed. The statistical difference is evaluated by one-way ANOVA followed by Tukey's multiple comparison
354 test. n=4 for each genotype. *Scale bars 1mm.*

355 **Disturbance of the TAM domain of SOX9 results in dose-dependent skeletal dysplasia in**
356 **young adult mice**

357 By postnatal (P) day 60 (P60), *Sox9*$^{del/del}$ mutant mice are adult-viable (Figure 5C). Dorsal X-
358 ray imaging showed normal segmentation and growth of the spine irrespective of genotype
359 (Figure 5, C-D). However, *Sox9*$^{del/del}$ mutant mice did display shorter femurs compared with
360 *Sox9*$^{del/+}$ and the wild-type mice (Figure 5D). We observed loss of the thoracic (T) 13 floating
361 ribs (100%, n=18; 8 male, 10 female) in *Sox9*$^{del/del}$ mice (Figure 5C', red asterisks; and Figure
362 4E), with the majority of *Sox9*$^{del/del}$ mice (94%) displaying bilateral loss of the T13 floating ribs
363 (Figure 5E). Notably, 16% of heterozygous *Sox9*$^{del/+}$ mice (n=25, 15 males, 10 females) also
364 displayed loss of either the right or left T13 floating rib (Figure 5C', red asterisk; and Figure
365 5E). In contrast, we never observed the loss of the T13 floating ribs in wild-type mice (n=8, 4
366 males, 4 females) (Figure 5, A' and E). Sagittal X-ray imaging showed that 43% of *Sox9*$^{del/del}$

mutant mice (n=7, 4 males, 3 females) showed ribcage defects at P60, which was not observed in wildtype (n=4, 2 males, 2 females) or *Sox9*$^{del/+}$ mice (n=8, 5 males, 3 females) (Supplemental Figure 6). Altogether, these results show that an in-frame microdeletion within the TAM domain of SOX9 causes spatially restrictive disruptions in the development of the axial and appendicular skeleton, some of which are hallmarks of acampomelic CMPD including loss of ribs, ribcage defects, and shortened long bones (14, 16).

Sox9$^{del/del}$ mutant mice also displayed an exacerbated kinked tail phenotype at P60 (Figure 5H). MicroCT imaging showed that tail kinks are associated with dysmorphic coccygeal vertebrae (Figure 5, H-H'''), including ectopic bone deposition in the marrow space in *Sox9*$^{del/del}$ mutant mice, bending of the vertebra, and fusion between vertebrae (Figure 5, H'-H''' and I). The bending and fusion of the caudal vertebrae in the *Sox9*$^{del/del}$ mice mimicked some phenotypes observed in the human patient with the Gly276Cys mutation (Figure 1E). Histological analysis of these kinked tail regions in *Sox9*$^{del/del}$ mice showed severe dysplasia of IVDs and growth plate (Figure 5, L-L'). In some regions, the nucleus pulposus was pushed toward the convex side of the curve, embedded within the annulus fibrosus layers (Figure 5L, yellow arrow). Some *Sox9*$^{del/del}$ mice also showed thinning and disruption of IVD endplate, characterized by loss of cellularity and lack of ossification in the endplate (Figure 5L') compared with the normal structure observed in wild-type and *Sox9*$^{del/+}$ mice (Figure 5, J-J' and K-K'). The vertebral growth plate within the kinked tail region is also disrupted, with disorganized cell columns and reduced proteoglycan staining in some regions of the growth plate (Figure 5L'), consistent with the reported reduction in proteoglycan staining in the IVDs of conditional SOX9 loss-of-function mice (6), further supporting our model that *Sox9*^{del} allele behaves as a mild hypomorphic allele. These results demonstrate that a microdeletion variant in the TAM domain of SOX9 is sufficient to cause the progressive onset of skeletal dysplasia

391 characterized by gross histological pathology of the IVDs, bending of the vertebral bodies, and

392 pathological changes of the growth plate.

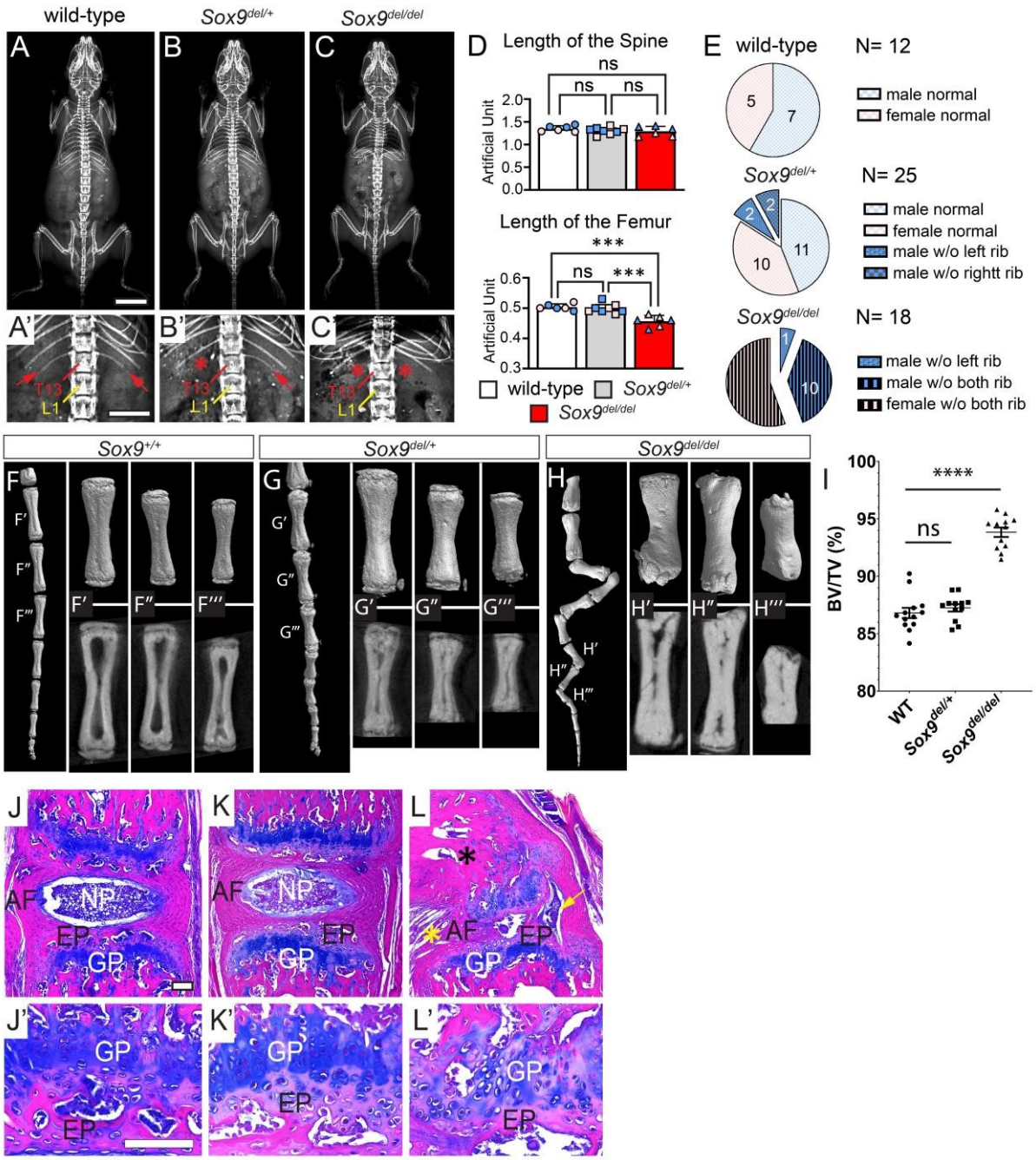

Figure 5. Variants in the TAM domain of SOX9 results in a dose-dependent skeletal dysplasia in adult mouse. (**A-C'**) Dorsal X-ray images of wild-type (**A, A'**), *Sox9*$^{del/+}$ (**B, B'**), and *Sox9*$^{del/del}$ mutant mice (**C, C'**) at P60. The presence and loss of T13 floating ribs are indicated with red arrows and red asterisks, respectively. (**D**) Measurements of the length of the spine (T1-L6) and the long bone (femur) in P60 mice. Bars are plotted with mean and 95%CI. Each dot represents one mouse analyzed. Male animals are marked with blue dots and female animals are marked with pink dots. The statistical analysis is one-way ANOVA followed by Tukey's multiple comparison test. ***p<0.001. ns: not significant. (n=6 for wild-type mice; 3 males, 3 females. n=8 for *Sox9*$^{del/+}$ mice; 4 males, 4 females. n=6 for *Sox9*$^{del/del}$ mice; 3 males, 3 females). (**E**) Quantification of the floating rib phenotype in P60 mice. (n=12 for wild-type mice; 7 males, 5 females. n=25 for *Sox9*$^{del/+}$ mice; 15 males, 10 females. n=18 for *Sox9*$^{del/del}$ mice; 8 males, 10 females). (**F-H**) MicroCT analyses showing 3D reconstruction of

the straight tails in wild-type (**F**) and *Sox9*$^{del/+}$ (**G**) mice, but kinked tail in *Sox9*$^{del/del}$ mice (**H**) at P60. Demonstrates a dose-dependent increase in attenuating bony matrix deposition in the bone marrow space in the optical sections of *Sox9*$^{del/+}$ and *Sox9*$^{del/del}$ mutant mice (lower panels: G'-G''' and H'-H''' respectively). (**I**) Analysis of percent bone volume (BV)/tissue volume (TV) of the 5-7th coccygeal vertebrae counting from the distal-most tip of the tail showing significant increase in BV/TV (%) in *Sox9*$^{del/del}$ mutant mice (p=<0.0001) compared with wild-ype control mice. Bars are plotted with mean and SEM. Each dot represents one coccygeal vertebra analyzed. The statistical difference is evaluated by one-way ANOVA followed by Tukey's multiple comparison test. n=4 mice for each genotype. (**J-L'**) ABH/OG staining performed on tail sections of P60 wild-type (**I, I'**), *Sox9*$^{del/+}$ (**J, J'**), and *Sox9*$^{del/del}$ (**K, K'**) mice showed severe disruption of IVD in *Sox9*$^{del/del}$ mice tails. The yellow arrow indicates nucleus pulposus tissue into the annulus fibrosus layer and a yellow asterisk indicates disorganization of the annulus fibrosus. n=3 for each genotype. *Scale bars: 10mm in **A**; 5mm in **A'**; 2mm in **F**; and 100μm in **I-I'**. AF: annulus fibrosus; EP: endplate; GP: growth plate; NP: nucleus pulposus.*

Disturbance of the TAM domain of SOX9 leads to late-onset scoliosis in mouse

We consistently observed skeletal dysplasia in the tails of *Sox9*$^{del/del}$ mutant mice from P5 to P60 but we never observed obvious dysplasia in the thoracic or lumber spine at this time (Figure 5, A-C). However, when we assessed these mutants at 6 month-of-age, ~ 43% of *Sox9*$^{del/del}$ mutant mice (n=14, 8 males, 6 females) displayed mild lateral curvature of the spine reminiscent of late-onset scoliosis (Figure 6, C and F). The severity of spine curvatures, quantified as Cobb angles (46), ranged from 10.2° to 13.8° (Figure 6I). We observed scoliosis in both male and female *Sox9*$^{del/del}$ mutant mice with curvatures in both rightward and leftward directions (Figure 6I). The distribution of the apex of the curvature was enriched in the lower thoracic region (T12-T13) and lumbar region (L1, L4, and L5) (Figure 6J). In comparison, only one female *Sox9*$^{del/+}$ mouse (n=15, 12 males, 3 females) showed a mild curve of 10.7° at 6 months (Figure 6H), while the majority of *Sox9*$^{del/+}$ mice and all of the wild-type mice (n=8, 4 males and 4 females) had no measurable scoliosis at 6 months (Figure 6G).

In addition, we also observed a range of rib cage deformities in 93% of the *Sox9*$^{del/del}$ mice at 6 months (n=14, 8 males, 6 females), from obvious dorsal ward bending of the sternums into the rib cage akin to pectus excavatum in humans (47) (Figure 6F'), to milder bending of the

sternums (Supplemental Figure 7, C and D) and curvatures of the distal ribs (Supplemental Figure 7E). We only observed 1 male *Sox9*$^{del/+}$ mice displaying mild bending of the sternum at 6 months (n=8, 4 males and 4 females) (Supplemental Figure 7B). In contrast, none of the wild-type littermates displayed rib cage deformities (n=8, 4 males and 4 females) (Figure 6D'). The etiology of pectus excavatum is still not clear, but it may be associated with genetic or connective tissue disease that leads to compromised support of the rig cage (48). These results suggest that disturbance of the TAM domain of *SOX9* also affects the stability of the axial skeleton during adult development, modeling late-onset scoliosis and progressive rib cage deformities in a dose-dependent manner, potentially through regulating the homeostasis of cartilaginous and connective tissues in the spine and rib cage.

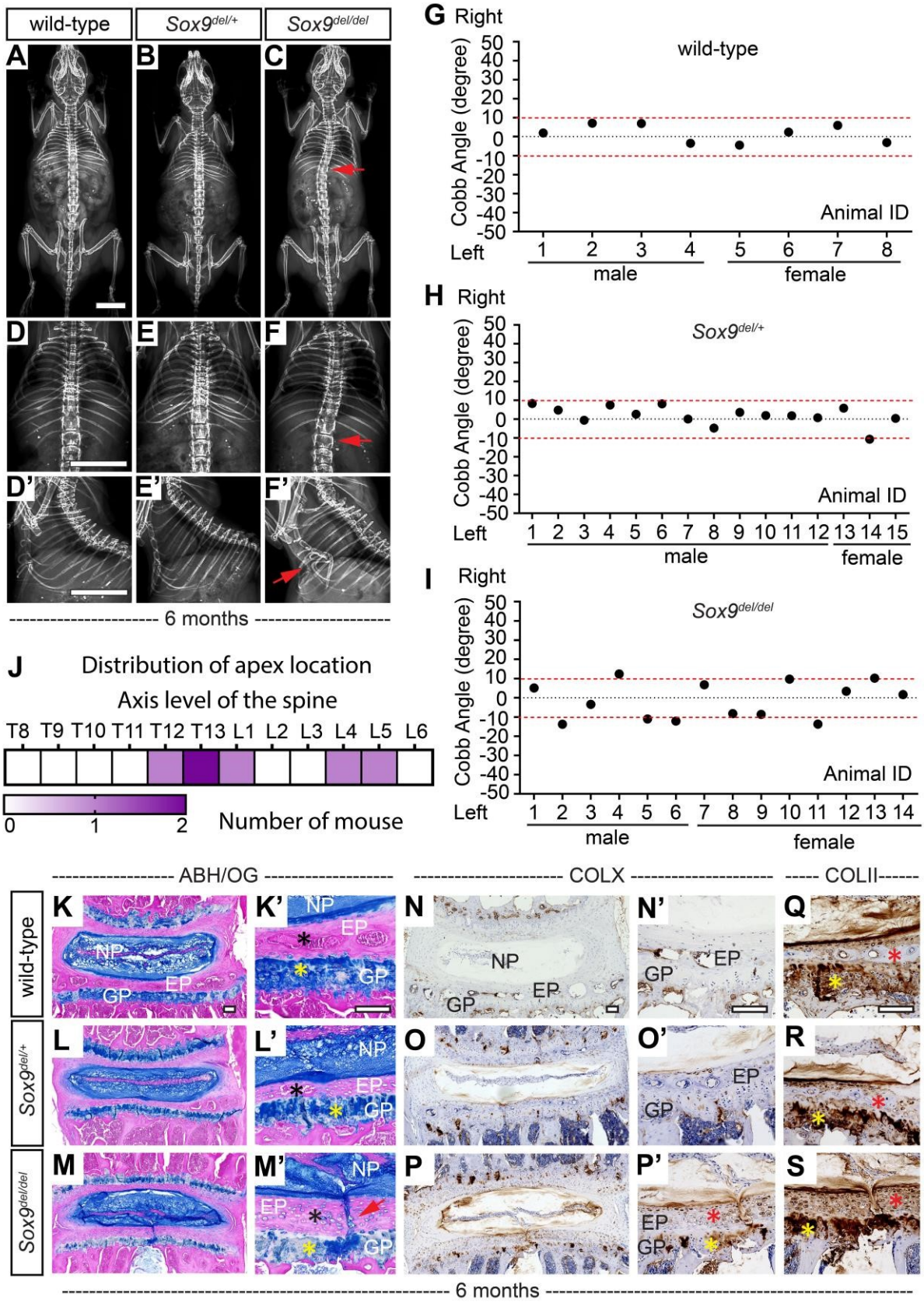

450

Figure 6. Adult *Sox9*$^{del/del}$ mutant mice display IVD defects of the spine. (**A-F'**) Representative dorsal X-ray images of wild-type (**A, D**), *Sox9*$^{del/+}$ (**B, E**) and *Sox9*$^{del/del}$ mutant mice (**C, F**) at 6 month-of-age. Sagittal X-ray images of the same mouse are shown in (**D'-F'**). Red arrows in (**C**) and (**F**) indicate scoliosis. The red arrow in

F' indicates rib cage deformity. (n=8 for wild-type mice; 4 males, 4 females. n=15 for *Sox9*$^{del/+}$ mice; 12 males, 3 females. n=14 for *Sox9*$^{del/del}$ mice; 8 males, 6 females.) (**G-I**) Cobb angle measurements of wild-type (**G**), *Sox9*$^{del/+}$ (**H**) and *Sox9*$^{del/del}$ (**I**) mice at 6 months. Areas of scoliosis (Cobb angle >10 degrees) are indicated with two red dot lines. (**J**) Heat map of the apex distribution of the scoliotic *Sox9*$^{del/del}$ mutant mice at 6 months. The heat map is plotted with the axis level of the thoracic spine (T8-L6) and the number of scoliotic mice with apex observed at each level. (n=8 for wild-type mice; 4 males, 4 females. n=15 for *Sox9*$^{del/+}$ mice; 12 males, 3 females. n=14 for *Sox9*$^{del/del}$ mice; 8 males, 6 females.) (**K-M'**), ABH/OG staining performed on lumbar IVDs (L4/5) of 6-month-old wild-type (**K, K'**), *Sox9*$^{del/+}$ (**L, L'**) and *Sox9*$^{del/del}$ (**M, M'**) mice. The endplate and growth plate are indicated with black and yellow asterisks, respectively. Endplate clefts observed in *Sox9*$^{del/del}$ mice are indicated with a red arrow in (**M'**) (n=3 for each genotype.) (**N-S**), Immunohistochemistry (IHC) analyses of type X collagen (COLX) and type II collagen (COLII) in 6-month-old wild-type (**N**, **N'** and **Q**), *Sox9*$^{del/+}$ (**O**, **O'** and **R**) and *Sox9*$^{del/del}$ (**P**, **P'** and **S**) mice. Endplate staining and growth plate staining are indicated with red and yellow asterisks, respectively. n=6 for each genotype. *Scale bars: 10mm in **A**, **D**, and **D'**; 100μm in **K-K'**, **N-N'**, and **Q**. EP: endplate; GP: growth plate; NP: nucleus pulposus.*

Adult *Sox9*$^{del/del}$ mutant mice display IVD defects of the spine

SOX9 function is required in adult mice to maintain homeostasis of the cartilaginous tissues (6, 49). To determine if *Sox9*$^{del/del}$ mutant mice might accumulate increased pathology of skeletal elements in older mice we looked at 6-month-old cohorts. We observed endplate defects in 50% (n=6) of *Sox9*$^{del/del}$ mutant mice (Figure 6, M-M'), characterized by vertical cleft through endplate into growth plate in the lumbar IVDs (Figure 6M', red arrow), which was not observed in *Sox9*$^{del/+}$ or wild-type littermates (n=6 for each genotype) (Figure 6, K-L'). We also observed reduced proteoglycan staining in some growth plates of the lumbar spine in the *Sox9*$^{del/del}$ mice (Figure 6M', yellow asterisk).

The endplates of the lumbar IVDs undergo ossification in wild-type adult mice (Figure 6, K' and 6L', black asterisks, and Supplemental Figure 7, F-G'). Interestingly, the *Sox9*$^{del/del}$ mice consistently displayed a reduction in endplate ossification in lumbar regions (Figure 6M' and Supplemental Figure 7J'), which was associated with an accumulation of COLX (+), hypertrophic chondrocyte-like cells in the endplate (Figure 6P', red asterisk; Figure 6M', black

asterisk, and Supplemental Figure 7, H' and I'). COLX is a biomarker of IVD degeneration (50, 51). We also observed increased COLX expression enriched around the endplate cleft and in the growth plate and nucleus pulposus of the *Sox9*$^{del/del}$ mice (Figure 6, P-P'), which suggests that reduction in SOX9 function is eliciting degenerative changes in the IVD. The ossification of the endplate in wild-type and *Sox9*$^{del/+}$ mice was also correlated with a reduction of COLII expression in the endplate (Figure 6, Q and R, red asterisks), however, COLII staining was increased in *Sox9*$^{del/del}$ mutant endplate (Figure 6S, red asterisks). The persistent expression of both COLII (Figure 6S) and COLX (Figure 6P') in large, hypertrophic chondrocyte-like cells in the endplate suggests that the TAM domain of SOX9 is important for pathways involved in chondrocyte maturation in the lumbar spine.

Variants of the TAM domain decrease SOX9 protein stability and chondrogenesis in cell culture

Next, we sought to determine how disturbance of the TAM domain affects SOX9 function. Consistent with our previous results with the human Gly276Cys *SOX9* TAM domain variant (Figure 2B), the luciferase assay showed that the Asp272del variant of *SOX9* showed no obvious change in transcriptional activity compared with the wild-type protein or the Gly276Cys variant (Figure 2B). Previous studies reported that phosphorylation of the TAM domain helps regulate SOX9 stability in response to DNA damage in cancer cells (52). We next sought to assay SOX9 protein stability by measuring the half-life of different SOX9 variants in Cos-7 cell culture after treatment with cycloheximide (CHX), which blocks *de novo* protein synthesis (53). Quantification of SOX9 revealed that the half-life of wild-type SOX9 was ~4 hours after CHX treatment, while the half-lives of both the human Gly276Cys and the mouse Asp272del variant of SOX9 proteins were reduced to ~2.5 hours (Figure 7, A and B, n=3).

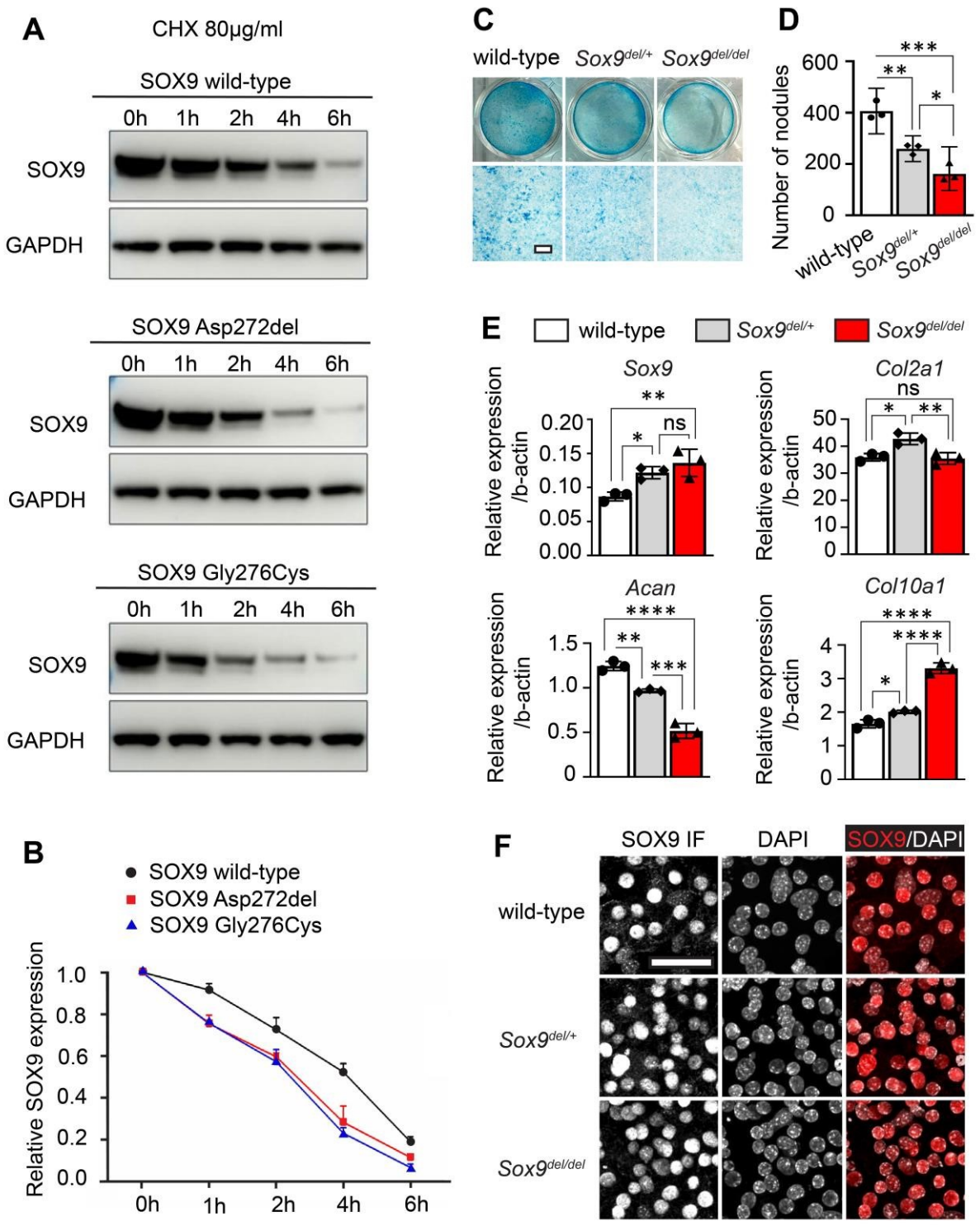

Figure 7. Variants of the TAM domain leads to reduced protein stability of SOX9 and impaired chondrogenesis in cell culture. (**A-B**) Representative Western blot assay of SOX9 half-life measurements (**A**). Cos-7 cells were transfected with plasmids expressing wild-type SOX9, the Asp272del variant, or the Gly276Cys variant for 48 hours, followed by cycloheximide (CHX) treatment (80 µg/ml) for 0h, 1h, 2h, 4h, and 6h. Total protein was harvested at each time point and blotted with SOX9. GAPDH was used as a loading control. Quantification of band intensity was shown in (**B**). (n=3 experiments.) (**C-D**), Alcian Blue staining (**C**) on costal chondrocytes isolated from P5 wild-type, *Sox9*$^{del/+}$, and *Sox9*$^{del/del}$ mice that were maturated for 10 days. The

number of nodules formed per tissue-culture well was quantified in (**D**). (n=3 experiments.) (**E**)**,** Real-time RT-PCR analyses of *Sox9*, *Col2a1*, *Acan*, and *Col10a1* on RNA isolated from P5 primary costal chondrocytes of three different genotypes. Bars are plotted with mean and 95%CI. Three pups of each genotype were pooled to generate a sample. Three technique replicas were applied for each experiment. The statistical difference is evaluated by one-way ANOVA followed by Tukey's multiple comparison test. * $p<0.05$, **: $p<0.01$, ***$p<0.001$. ***$p<0.0001$. ns: not significant. (**F**)**,** Immunofluorescence (IF) analyses of SOX9 performed on P5 primary costal chondrocytes of three different genotypes revealed comparable expression levels and normal nuclei localization of the SOX9 Asp272del variant protein. (n=3 experiments.) *Scale bars: 500μm in **C**; 50μm in **F**.*

Given the pathology of cartilaginous tissues in the IVD in $Sox9^{del/del}$ mutant mice, we next sought to test if primary costal chondrocytes would also model these defects in vitro. Alcian Blue staining on maturated primary costal chondrocytes revealed weaker Alcian Blue staining and a reduction in cartilage nodules formation of chondrocytes derived from both $Sox9^{del/+}$ and $Sox9^{del/del}$ mice compared with that derived from wild-type littermates (Figure 7, C and D), suggesting diminished chondrogenesis in vitro (54) with the Asp272del TAM domain variant of *SOX9*. This observation is confirmed by the reduced expression of *Acan* (Figure. 7E), which encodes the major chondroitin sulfate proteoglycan aggrecan and its deposition is considered a hallmark of chondrogenesis (55). In agreement with our observations of increased COLX expression in cartilaginous endplate in $Sox9^{del/del}$ mutant mice (Figure 6, P-P'), we also observed increased *Col10a1* expression in primary costal chondrocyte culture in both $Sox9^{del/+}$ and $Sox9^{del/del}$ mice (Figure 7E). These findings indicate that the Asp272del TAM domain variant of *SOX9* is driving cell autonomous, precocious hypertrophy signaling in chondrocytes. Similar alterations in gene regulation have been previously observed in the *Sox9* haploinsufficiency mice, where the overall markers of chondrogenesis were inhibited, yet are also coupled with increased expression of markers of hypertrophy and mineralization (23, 56).

Col2a1 is a direct transcriptional target of SOX9 (28), however, *Col2a1* expression was not obviously changed in costal chondrocytes derived from $Sox9^{del/+}$ or $Sox9^{del/del}$ mice (Figure 7E), which is consistent with our analysis of COLII in vivo (Supplemental Figure 4, C-E). We

observed increased *Sox9* mRNA level in costal chondrocytes of $Sox9^{del/+}$ and $Sox9^{del/del}$ mice compared with that in wild-type cells (Figure 7E), likely the result of SOX9 positive feedback on its expression (57). Despite increased *Sox9* transcript levels, we failed to observe any obvious changes in the expression or localization of the SOX9 protein by immunofluorescence or western blotting in primary costal chondrocytes (Figure 7F and Supplemental Figure 8). These results suggest a potential complementation effect driving *Sox9* mRNA overexpression in response to the hypomorphic loss of function of the TAM domain microdeletion in *SOX9*, which was consistent with our previous observations of decreased SOX9 protein stability (Figure 7, A and B).

Disturbance in of the TAM domain of SOX9 generates global transcriptional changes in chondrocytes and altered protein expression in spinal tissues

Our results show that variants in the TAM domain of *SOX9* lead to the compromised formation of the intervertebral discs (Figure 3G and Figure 5L), altered ossification in the endplates (Figure 6, M, P and S), and decreased chondrogenesis in cell culture (Figure 7, C-E). All of this data suggests that variants in the TAM domain of *SOX9* have a crucial role in the differentiation and maturation of the cartilage lineages. To better understand how the Asp272del variant affects gene regulation, we performed RNA-sequencing analyses on P5 primary costal chondrocytes, a well-accepted source of primary chondrocytes (58, 59). We observed a total of 816 upregulated genes and 452 down-regulated genes in homozygous $Sox9^{del/del}$ compared to heterozygous $Sox9^{del/+}$ mutant mice (Figure 8A and Supplemental Table 3). Gene Ontology (GO) enrichment analysis revealed that the differentially expressed genes were strongly related to extracellular matrix (GO:0031012), angiogenesis (GO:0001525), and ossification (GO:0001503) (Supplemental Table 4). Other altered biological processes included connective

565 tissue development (GO:0061448), cell-substrate adhesion (GO:0031589), and epithelial cell
566 migration (GO:0010631) (Supplemental Table 4).

567 We observed global alterations in components of the extracellular matrix, including
568 increased expression of *Col8a1* (type VIII collagen), *Eln* (elastin), and *Prg4* (proteoglycan 4),
569 and mild upregulation of *Col10a1* (type X collagen) (Figure 8B), which is consistent with our
570 observations of increased *Col10a1*/COLX expression in vivo (Figure 6, P-P') and in primary
571 chondrocyte culture (Figure 7E). On the contrary, the expression of some fibrotic collagens,
572 including *Col3a1* and *Col4a1* was significantly reduced (Figure 8B). Additional extracellular
573 matrix components, such as *Tnxb* (tenascin-X), *Tnc* (tenascin-C) and *Lama2* (laminin subunit
574 alpha 2) were also down-regulated. In addition, several genes involved in angiogenesis such as
575 *Vegfa* were upregulated. Finally, we observed intriguing results in a class of genes associated
576 with ossification. We found reduced expression of some major markers of ossification,
577 including *Col1a1*, *Mmp13,* and *Postn* (periostin, osteoblast specific factor), and increased
578 expression of *Timp3* (tissue inhibitor of metalloproteinase 3) (Figure 8B). These results may
579 explain the progressive, high penetrance (93%) of the rib cage deformities in the $Sox9^{del/del}$ mice
580 (Figure 6F'), which may be caused by impaired ossification of the rib cage. This dysregulation
581 of genes important for endochondral ossification is also consistent with the loss of endplate
582 ossification observed within the lumbar IVDs of the $Sox9^{del/del}$ mice (Figure 6, M-M'). We also
583 observed increased expression of the bone morphogenetic protein (BMP) and transforming
584 growth factor-β (TGFβ) pathways, including *Bmp6*, *Smad5,* and *Tgfbr3*, coupled with up-
585 regulation of some BMP signaling inhibitors, such as *Nog* (Noggin) and *Grem1* (gremlin, 1
586 DAN family BMP antagonist) (Figure 8B). Collectively, these results show large-scale
587 dysregulation of genes that are important for chondrocyte differentiation and ossification in
588 $Sox9^{del/del}$ mice.

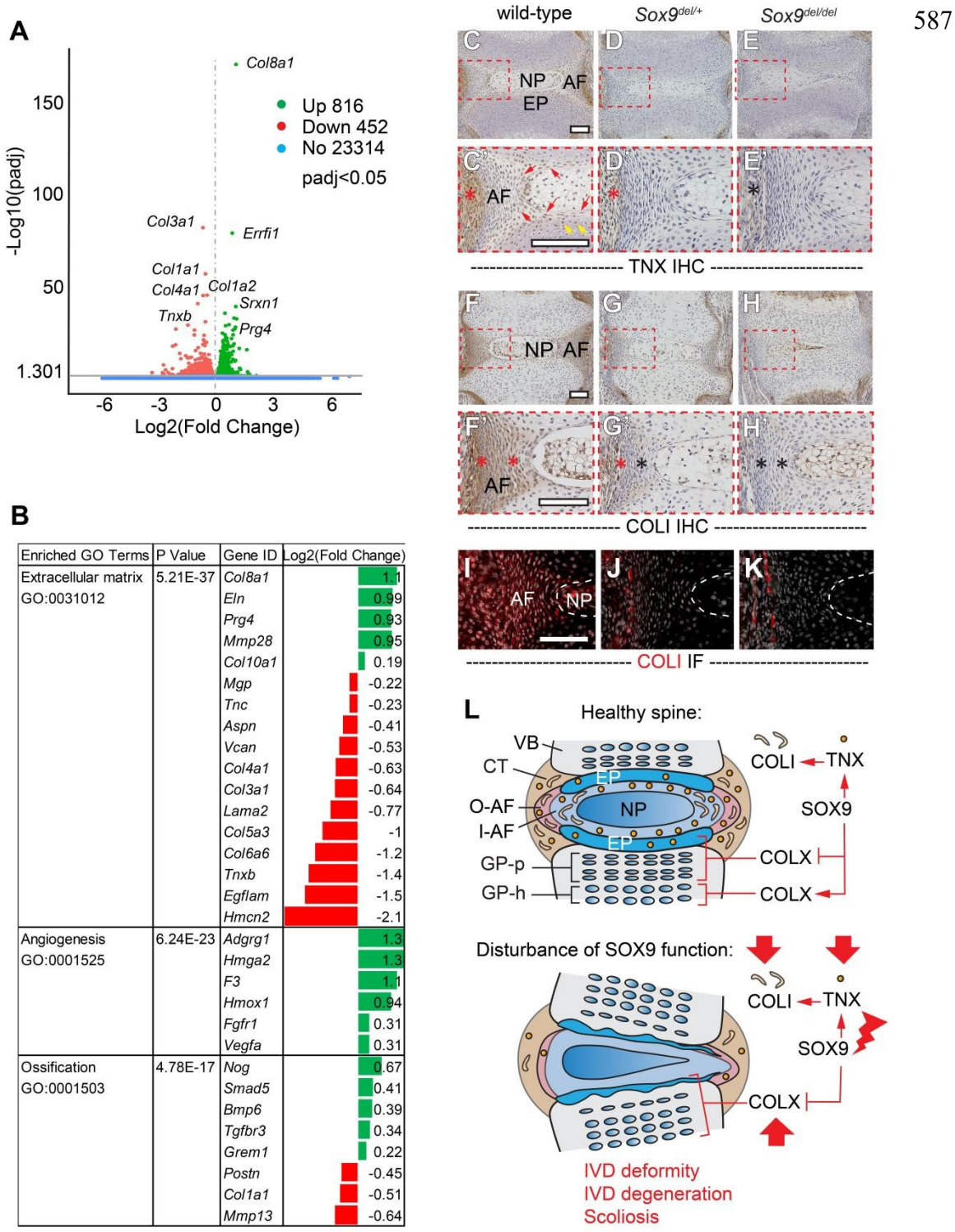

B

Enriched GO Terms	P Value	Gene ID	Log2(Fold Change)
Extracellular matrix GO:0031012	5.21E-37	*Col8a1*	1.1
		Eln	0.99
		Prg4	0.93
		Mmp28	0.95
		Col10a1	0.19
		Mgp	-0.22
		Tnc	-0.23
		Aspn	-0.41
		Vcan	-0.53
		Col4a1	-0.63
		Col3a1	-0.64
		Lama2	-0.77
		Col5a3	-1
		Col6a6	-1.2
		Tnxb	-1.4
		Egflam	-1.5
		Hmcn2	-2.1
Angiogenesis GO:0001525	6.24E-23	*Adgrg1*	1.3
		Hmga2	1.3
		F3	1.1
		Hmox1	0.94
		Fgfr1	0.31
		Vegfa	0.31
Ossification GO:0001503	4.78E-17	*Nog*	0.67
		Smad5	0.41
		Bmp6	0.39
		Tgfbr3	0.34
		Grem1	0.22
		Postn	-0.45
		Col1a1	-0.51
		Mmp13	-0.64

Figure 8. The Asp272del TAM domain variant of SOX9 generates global transcriptional changes in chondrocytes and altered protein expression in spinal tissues of the IVD. (**A**) Volcano plot of RNA-sequencing data generated from P5 primary costal chondrocytes, plotted with Log2 (Fold Change) (X axis) and Log10 (padj)(Y axis, padj<0.05). Several top-changed genes were labeled on the plot. (n=3 replicas for each genotype.) **(B),** A

list of candidate genes involved in the top three categories of GO term enrichment analyses. **C-H',** Immunohistochemistry (IHC) analyses of tenascin X (TNX) and type I collagen (COLI) in P5 tail sections of wild-type (**C, C'** and **F, F'**), *Sox9*$^{del/+}$ (**D, D'** and **G, G'**) and *Sox9*$^{del/del}$ (**E, E'** and **H, H'**) mice. TNX expression in connective tissues (red asterisks), inner annulus fibrosus (red arrows), and endplate (yellow arrows) are shown in (**C'**). Loss of TNX expression in connective tissues is indicated with a black asterisk in (**E'**). The presence or loss of COLI staining in annulus fibrosus is indicated with red or black asterisks respectively in (**F'-H'**). (n=6 for each genotype.) **I-K,** Immunofluorescence (IF) analyses of COLI were performed on P5 mouse tail sections of three different genotypes. (n=6 for each genotype.) **L,** A model of how SOX9 regulates axial skeleton homeostasis. In a healthy spine, SOX9 maintains normal expression of TNX and COLI in annulus fibrosus, connective tissues and cartilaginous tissues, and precisely controls the expression of COLX in chondrocytes. However, disturbance of SOX9 function results in reduced expression of TNX and COLI in connective tissues and dysregulated expression of COLX in the endplate and growth plate of the spine, which synergistically results in a range of skeletal dysplasia, including intervertebral disc (IVD) deformity, IVD degeneration, and scoliosis. *Scale bars: 100μm. VB: vertebral body; CT: connective tissue; EP: endplate; NP: nucleus pulposus; GP-p: proliferative growth plate; GP-h: hypertrophic growth plate; AF-i: inner annulus fibrosus; AF-o: outer annulus fibrosus*.

In humans, disruption of the *TNXB* gene (which encodes tenascin-X, TNX, an extracellular matrix protein) is associated with Ehlers-Danlos syndrome, which is a connective tissue disorder caused by defective deposition of type I collagen leading to hypermobility of joints and kyphoscoliosis in some patients (60, 61). Since we observed reduced expression of both *Tnxb* and *Col1a1* in primary chondrocyte cultures prior to the onset of scoliosis, we next set out to assay the expression of TNX and COLI in vivo. IHC analyses on P5 wild-type tail sections showed strong TNX expression in the inner annulus fibrosus (Figure 8, C-C', red arrows), a portion of cells in the endplate (Figure 8C', yellow arrows), and the connective tissues surrounding the annulus fibrosus (Figure 8C', red asterisk). However, the expression of TNX was consistently diminished in both *Sox9*$^{del/+}$ and *Sox9*$^{del/del}$ mice (Figure 8, D' and E'), with only weak staining in the connective tissues adjacent to IVD in the *Sox9*$^{del/+}$ mice (Figure 8D', red asterisk). Similarly, IHC and IF analyses revealed robust COLI expression in the entire annulus fibrosus and adjacent connective tissues of the wild-type mice (Figure 8, F-F', red asterisks; and Figure 8I), which is depleted in both *Sox9*$^{del/+}$ and *Sox9*$^{del/del}$ mice (Figure 8, G

622 and H'), with limited expression in the outer annulus fibrosus (Figure 8G', red asterisk; and
623 Figure 8J-K). Interestingly, the diminished expression of TNX and COLI in annulus fibrosus
624 overlaps altered SOX9 expression in annulus fibrosus (Figure 3, H''-J'''), suggesting a
625 regulatory role of SOX9 in maintaining the proper expression of these genes in the IVD.
626 Altogether, this finding suggests that disturbance of the TAM domain allows for normal
627 skeletal development to occur but still results in the loss of components, such as TNX and
628 COLI, that are likely necessary for the maturation and homeostasis of the spine (Figure 8L).
629

630

DISCUSSION

Heterozygous mutations in *SOX9* cause CMPD, a rare, dominant semi-lethal skeletal disease characterized by congenital shortening and bending of long bones. Most of the variants that cause CMPD are non-truncating mutations in HMG and DIM domains or truncating mutations in PQA and TAC domains (31-33). Notably, variants associated with acampomelic CMPD, a subpopulation of CMPD patients that exhibit milder skeletal phenotypes without displaying bending of long bones, are more likely to be either missense mutations of *SOX9* or deletions or rearrangements upstream of the *SOX9* coding region (34, 38). These observations suggest that locations and the nature of the variants may underlie the severity of CMPD/ acampomilic CMPD.

We recently reported a non-truncating pathological variant in the TAC domain which is associated with a milder form of axial skeleton dysplasia (35). Here, we reported the first non-truncating pathological variant in the TAM domain of *SOX9*. Patient with this variant exhibit skeletal dysplasia that primarily affects the axial skeleton and is milder than CMPD/acampomelic CMPD. Our studies suggest that non-truncating *SOX9* variants in the middle (TAM) or C-terminal transactivation domains (TAC) of SOX9 may contribute to skeletal dysplasia that is milder than classic CMPD/acampomelic CMPD, in which they affect primarily or exclusively the axial skeleton. These two studies corroborate with in vitro evidence suggest that the two transactivation domains of SOX9 can work synergistically to control the function of SOX9 (8).

Though the function of SOX9 in different skeletal tissues is well studied in mice (23), the molecular, cellular, and developmental abnormalities leading to CMPD/ acampomilic CMPD, especially the milder form of axial skeletal dysplasia, are not well defined, largely due to the lack of human evidence and appropriate animal models (24). In the present study, we analyzed

exome sequencing from 424 congenital vertebral malformations cases, a cohort of patients with a broad spectrum of syndromic and non-syndromic vertebral malformations. The inclusion of patients with milder skeletal phenotypes enabled us to identify four novel ultra-rare *SOX9* variants. We demonstrated that these variants were deleterious and provided acampomelic CMPD diagnosis for two of the patients who carry *de novo* variants in the HMG domain of *SOX9*. The identification of these two variants expands the mutational spectrum of *SOX9* in acampomelic CMPD and conforms that the hypomorphic *SOX9* allele that perturbs its DNA binding ability contributes to acampomelic CMPD. Another variant is in the DIM domain and leads to compromised SOX9 dimerization, which is consistent with previous analyses of DIM domain mutations (19).

For the first time, we identified a missense mutation, Gly276Cys, in the TAM domain of *SOX9*. The patient carrying this variant exhibited milder phenotypes than that of classical CMPD/ acampomelic CMPD, with multiple fusions of the thoracic vertebral and clinodactyly of the distal 5th phalange. Unlike the three variants identified in HMG and DIM domains, the mutation in the TAM domain does not obviously affect the transcriptional activity of canonical direct SOX9 targets but leads to reduced protein stability of SOX9. A previous study using cancer cells shows that the S*OX9* TAM domain plays an important role in the cellular response to DNA damage. A conserved phosphodegron (CPD) motif locates within the TAM transactivation domain is essential for the binding of FBW7α to SOX9, which is required for subsequent ubiquitination and proteasomal destruction of the SOX9 protein (52). Our study confirms that TAM domain is also involved in the regulation of SOX9 stability in chondrogenic lineages, however, the mechanisms of how specific amino acid residues in TAM domain regulate the turnover of SOX9 protein warrants further investigation.

Since no non-truncating variants in the TAM domain of SOX9 has been previously reported, we engineered a new mice model (*Sox9*$^{del/del}$) resulting in an in-frame microdeletion

of a single amino acid in the TAM domain (Asp272del), which is four residuals upstream of the human variant (Gly276Cys). Though we were not able to generate the exact human mutation, the *Sox9*^{del} allele also provides us with valuable information to understand the role of the TAM domain in *SOX9* function and the etiology of a milder form of axial skeleton dysplasia. *In silico* analyses show that the Asp272 and Gly276 residues are highly conserved among vertebrate orthologues, and both are predicted to hydrogen bond interact with Asp274 to stable a putative helical structure of the SOX9 protein. In addition, the Asp272del variant also shows adequate luciferase activity and reduced protein stability that is comparable with the Gly276Cys variant. We further demonstrate that *Sox9*^{del} is a hypomorphic allele with the genetic complementary experiment over a conditional *Sox9* null allele (*Sox9*^{flox}). These observations suggest that the *Sox9*^{del} allele may serve as a good genetic mouse model to study the function of the TAM domain and the pathogenesis of milder forms of axial skeletal dysplasia.

Interestingly, the homozygous *Sox9*$^{del/del}$ mutant mice display axial skeleton phenotypes that phenocopy some of the dysplasia observed in the human patient with the Gly276Cys variant, but not in mouse models with typical null or haploinsufficiency of *Sox9* (3, 23). For example, the *Sox9*$^{del/del}$ mutant mice display bending and fusion of some caudal vertebrae without displaying bending of the long bones. The *Sox9*$^{del/del}$ mutant mice also show loss of T13 floating ribs, rib cage dysmorphologies, pathoses of IVD and growth plates, and late-onset scoliosis without congenital vertebral malformations. In contrast, haploinsufficiency of *Sox9* results in more severe forms of skeletal dysplasia and defective cartilage development (14, 23, 38). On the other hand, the *Sox9*$^{del/+}$ mutant mice show much milder skeletal phenotypes compared with *Sox9*$^{del/del}$ and *Sox9* haploinsufficiency mice. All these observations confirm that *Sox9*^{del} is a mild hypomorphic allele with no dominant-negative impact as reported in other *SOX9* truncating variants (24). Though *Sox9*^{del} does not obviously affect the expression of

SOX9 protein at the tissue level (Supplemental Figure 8, Western blot of primary chondrocytes) or significantly reduce its transcriptional activity, the function of SOX9 may be compromised by reduced protein stability. Therefore, the hypomorphic *Sox9*^{del} allele may permit some transcriptional activity at the canonical SOX9 targets and allows for normal skeletal development to occur, however, it may lead to compromised tissue development and maintenance during neonatal and adult development, such as reduced proliferation of the endplate in P5 IVD, and reduced proteoglycan staining of the vertebral growth plate in adult mice, which is consistent with the previous finding on the crucial role of SOX9 in disc cell survival and phenotype maintenance, and in the regulation of distinct compartment-specific transcriptomic landscapes (6, 7).

Moreover, IHC analysis on tissue sections shows that the expression of SOX9 is reduced in distinct regions of the cartilaginous and connective tissues of the spine (Figure 3, P5 tail). RNA-seq performed on costal chondrocytes at the same age revealed that *Sox9*^{del} mutation causes reduced expression of extracellular matrix components, and alterations in angiogenesis and ossification pathways. SOX9 is known to have a direct role in the establishment of tendon and ligament attachments and indirectly for endochondral ossification (2, 5), thus the role of SOX9 TAM variants on the development and homeostasis of bone and dense connective tissues should be further studied.

One possible mechanism of wedged IVD observed in P5 *Sox9*$^{de/dell}$ mice is that the altered extracellular matrix components (e.g. abnormally decreased expression of TNX and COLI) lead to altered biomechanical properties of the disc, while the increased expression of type X collagen and dysregulated ossification process within the vertebrae, probably due to the reduced expression of *Col1a1* and *Mmp13* (Figure 8B) and reduced proliferation within the proliferative growth plate (Figure 3Q), synergistically leads to disc deformity (Figure 8L). We also observe signs of disc degeneration in older *Sox9*$^{de/dell}$ mice, including reduced proteoglycan staining and

730 endplate abnormalities. Our study adds support to previous studies showing that SOX9 is
731 essential for spine development and maintenance of the structural integrity of the spine (3, 6,
732 7, 49). Interestingly, we observed a similar endplate phenotype in another genetic mouse model
733 (*Adgrg6* conditional knockout) that was published earlier by our group (62). In *Adgrg6*
734 conditional mutant mice, we suggest that the endplate-oriented phenotype is a secondary effect
735 due to compromised biomechanical properties of the IVD because of altered expression of
736 extracellular matrix components, including reduced expression of SOX9 but increased
737 expression of type X collagen (62, 63). In this study, we observed similar alterations in
738 $Sox9^{del/del}$ mice, where we showed SOX9 expression is regionally reduced, increased expression
739 of type X collagen in the endplate and growth plate, supporting a potential synergistic
740 interaction between SOX9 and ADGRG6, which is implicated in adolescent idiopathic scoliosis
741 in humans (64).

742 Taken together, our results demonstrate adult viable skeletal dysplasia phenotypes
743 including scoliosis and malformation of the distal axial skeleton in mice and humans, due to
744 novel pathological mutations localized within the TAM domain of *SOX9*. Disturbance of the
745 *SOX9* TAM domain in mice and in human patient showed axial skeletal malformations without
746 generating more severe skeletal dysplasia and autosomal sex reversal phenotypes, which are
747 commonly associated with known CMPD/ acampomilic CMPD *SOX9* mutations in humans.
748 Our study corroborates previous evidence from human and mouse studies that *SOX9* has critical
749 roles in axial skeleton formation and adult homeostasis and that *SOX9* hypomorphic alleles
750 resulting from variants in the TAM or TAC domain likely underlie skeletal dysplasia that is
751 milder than CMPD/ acampomilic CMPD, which primarily or exclusively affect the axial
752 skeleton. In conclusion, human and mouse variants in *SOX9* contribute to a range of skeletal
753 dysplasia dependent on the domain/residual affected, which is suggestive of a general
754 mechanism to be further explored in skeletal dysplasia in humans.

MATERIALS AND METHODS

Human subjects

A total of 424 probands with congenital vertebral malformations admitted into Peking Union Medical College Hospital (PUMCH) were consecutively enrolled under the framework of the Deciphering disorders Involving Scoliosis and COmorbidities (DISCO) study (http://www.discostudy.org/) from 2009 to 2016. Clinical evaluation and exome sequencing were performed as previously described (65). Raw data were processed using the in-house developed Peking Union Medical College Hospital Pipeline (PUMP) (65, 66). Ultra-rare variants in *SOX9* were selected based on the following criteria: 1) Predicted to alter the protein sequence; 2) Either arising *de novo* or absent from the public databases such as the genome aggregation database (gnomAD, https://gnomad.broadinstitute.org/). Patients carrying candidate variants in *SOX9* are reported in this study.

Sanger sequencing

For human patients and mouse models, candidate variants in *SOX9*/*Sox9* were validated by Sanger sequencing. For human patients, variant-encoding amplicons were amplified by PCR from genomic DNA obtained from probands and parents from trios (Supplemental Table 1). The amplicons were purified using an Axygen AP-GX-50 kit (lot no. 05915KE1) and sequenced by Sanger sequencing on an ABI3730XL instrument.

Construction of *SOX9* expression constructs and Cos-7 cell culture

Full-length wild-type *SOX9* and *SOX9* with variants were cloned into the pEGFP-C1 expression vector (Catalog #6084-1, Takara Bio Company). Cos-7 cells were obtained from the Institute of Basic Medical Sciences, Chinese Academy of Medical Sciences (Beijing, China). The cells

were cultured in DMEM medium (Gibco) supplemented with 10% fetal bovine serum (Gibco), penicillin (50 U/ml, Life Technology), and streptomycin (50 μg/ml, Life Technology).

Electrophoretic mobility shift assay

Electrophoretic mobility shift assay (EMSA) was used to detect the binding affinity of SOX9 proteins to the conical SOX9 binging motifs as previously described with modifications (19). Biotin-labeled DNA probes were designed based on two canonical SOX9 binding motifs derived from an enhancer region of the mouse *Col11a2* gene, named *Col11a2* B/C and D/E respectively, according to the original publication (19). The sequences of these motifs are listed in Supplemental Table 2. Cos-7 cells were transfected with the SOX9 expression constructs or GFP control construct for 48 hours. The expression level of wild-type and various SOX9 mutant proteins was quantified by Western blot before the experiment and equal amounts of SOX9 were detected (Supplemental Figure 2). After 48 hours, the whole-cell lysates were extracted and incubated with 0.5 μl of Biotin-labeled probe (1000fM) for 20 min on ice in a 15μl reaction system as described previously (19), using Poly (dI:dC) as the unspecific competitor. The 150-fold unlabeled DNA probes (150X) were incubated with cell lysate of Cos-7 cells transfected with wild-type SOX9 protein. Samples were loaded onto native 6.5% polyacrylamide gel and electrophoresed in 0.5xTBE at 180V for 1 h. The gel was transferred to a nylon membrane at 100V for 30 min. The biotin-labeled DNA probes transferred to the membrane were cross-linked for 10 min with a hand-held UV lamp and detected by Chemiluminescence (BioRad, TY8836).

Luciferase assay

Luciferase assay was performed with a luciferase reporter (*Col11a2*-Luc) and various *SOX9* expression constructs in Cos-7 cell cultures. To generate the *Col11a2*-Luc reporter, four tandem copies of a canonical SOX9 binding motif derived from an enhancer region of the

mouse *Col11a2* gene (named *Col11a2* D/E) (19) was cloned into the luciferase reporter vector pGL3Basic (Promega E1751). The sequence of this motif is listed in Supplemental Table 2. Full-length wild-type *SOX9* and *SOX9* with variants were cloned into the pEGFP-C1 expression vector (Catalog #6084-1, Takara Bio Company). These overexpression constructs were transfected into the Cos-7 cell line for 48 hours and equal amounts of protein were harvested for Western Blotting analysis of SOX9. No obvious difference in SOX9 expression was observed among wild-type and different *SOX9* variants (Supplemental Figure 3, A and B). A standard curve was generated to determine the linear range of the SOX9-mediated reporter transactivation and to optimize the reaction system (Supplemental Figure 3C). For each independent experiment, Cos-7 cells were transfected with 400ng of *Col11a2*-Luc reporter plasmids, 50ng of various SOX9-expression vectors, and 5ng of Renilla luciferase control reporter vectors. Cells were harvested 48h post-transfection for immediate luciferase activity analysis using the Promega Dual-Luciferase Reporter Assay System (Promega E1910). The Firefly luciferase activity was normalized to the Renilla luciferase activity. Three independent experiments were performed with reproducible results.

Half-life measurement

The half-life of wild-type and variant SOX9 proteins were evaluated using a cycloheximide (CHX) chase assay. Cos-7 cells were seeded into 6-well plates in DMEM containing 10% FBS and transfected with 2 μg of various *SOX9* expression constructs. 48 hours later, Cos-7 cells were treated with 80 μg/ml of CHX and were harvested at 0h, 1h, 2h, 4h, and 6h after treatment. Cells were dissolved in absolute ethanol and harvested in ice-cold phosphate-buffered saline (PBS, pH 7.4) by centrifuging at 2500 × g for 2 min at 4 °C. Cell pellets were lysed in RIPA lysis and extraction buffer (Thermo Scientific) and sonicated for 3 × 5 s on ice. Total protein from the cell lysate was quantitated using the Pierce BCA protein assay kit (Thermo Scientific) and analyzed by the standard Western blot assay. The membrane was blotted with a primary

826 anti-GFP tag antibody (Cell Signaling Technology, 2956T, 1:1000) and detected with a
827 secondary horseradish peroxidase-conjugated antibody (ab7090; Abcam; 1:5000).
828 Quantification of band intensity was conducted using Image Lab (BioRad). Three independent
829 experiments were performed with reproducible results.

830 **Generation of mouse models**

831 The *Sox9* ^{Asp272del} mutant mouse was fortuitously isolated after pronuclear injection using an
832 oligo-dependent gene editing approach using a single CRISPR synthetic guide RNA 5'-
833 GTTCACCGATGTCCACGTCG-3' (Synthego) mixed with Alt-R S.p. HiFi Cas9 Nuclease
834 V3 protein (IDT, 1081060). For gene editing, a donor oligonucleotide 5'-
835 TCTGGCAGAGGGGGGCAGACAGCCCCCCATCGACTTtCGtGAtGTaGAtATCtGcG
836 AACTGAGCAGCGACGTCATCTCCAACATTGAGACCTT-3', with phosphorothioate
837 linkages between the first three and last three nucleotides, was used to induce a specific edit to
838 model the Gly276Cys human mutation and add synonymous changes to include an EcoRV
839 restriction site for genotyping. The pronuclear injection was performed by the Mouse Genetic
840 Engineering Facility (UT-MGEF) at the University of Texas at Austin using standard protocols
841 (https://www.biomedsupport.utexas.edu/transgenics). Of the 123 implanted embryos from two
842 independent sessions, 3 mice were isolated at sexual maturity. Of these, 1 founder male
843 transmitted the *Sox9* ^{Asp272del} allele. Locus-specific genotyping of the *Sox9* ^{Asp272del} mutation was
844 performed using PCR primers 5'-GTCTTTCTCTTTTATGGCCTGC-3'and
845 5'TGGCAAGTATTGGTCAAACTCA-3', followed by Sanger sequencing confirmation.
846 Heterozygous *Sox9* ^{Asp272del} mutant mice are maintained in the C57B6/J background and have
847 been outcrossed to the C57BL/6J strain for over 10 generations. At each cross, we observe a
848 100% correspondence between genotype and phenotype.

849 **Analysis of mouse tissues**

850 Radiographs of the mouse skeleton were generated using a Kubtec DIGIMUS X-ray system
851 (Kubtec T0081B) with auto exposure under 25 kV. All radiographs were taken immediately
852 after the mice were euthanized to avoid the stiffness of the skeleton. Cobb's angle was measured
853 on high-resolution X-ray images with the software Surgimap (https://www.surgimap.com), as
854 previously described by (46). Measures of the length of the spine (T1-L6) and long bone (femur)
855 were performed on high-resolution X-ray images with ImageJ (https://imagej.nih.gov/ij/).

856 Mouse spine or tail tissues were harvested at P5, P60, and 6 months of age. Histological
857 analysis was performed on the distal tail or lumbar (L3-L5) spines fixed in 10% neutral buffered
858 formalin for 3 days at room temperature, followed by 3-5 days of decalcification in Formic
859 Acid Bone Decalcifier (Immunocal, StatLab). After decalcification, bones were embedded in
860 paraffin and sectioned at 5μm thickness. Alcian Blue Hematoxylin/Orange G (ABH/OG)
861 staining was performed following standard protocols (Center for Musculoskeletal Research,
862 University of Rochester). Immunohistochemical (IHC) analyses were performed on paraffin
863 sections with traditional antigen retrieval (COLII and COLX: 4 mg/ml pepsin in 0.01 N HCl
864 solution, 37°C water bath for10 min; SOX9 and Collagen I: 10 μg/ml proteinase K in 1x PBS,
865 room temperature for 10 min; TNX: 10 mM Tris-EDTA with 0.05% Triton-X-100, pH 9.0,
866 75°C water bath for 5 min) and colorimetric developed development methodologies with the
867 following primary antibodies: anti-SOX9 (EMD Millipore AB5535, 1:200), anti-COLII
868 (Thermo Scientific MS235B, 1:100), anti-COLX (Quarteet, 1-CO097-05, 1:200), anti-COLI
869 (Abcam, ab138492, 1:1000), and anti-TNX (Santa Cruz Biotechnology sc-271594, 1:100).
870 Immunofluorescence (IF) staining was performed on paraffin sections as previously described
871 with modifications (67). Briefly, paraffin sections of P5 mouse tails were de-paraffinized and
872 incubated with 10 μg/ml proteinase K in 1x PBS at room temperature for 10 min. Sections were

washed in 1xPBST and incubated with primary antibodies: anti-SOX9 (Chemicon AB5535, 1:200) and anti-TNX (Santa Cruz Biotechnology sc-271594, 1:100), and developed with secondary antibody Alexa Flour 488 Goat anti Rabbit (A11034, 1:1500). Images were taken using a Keyence BZ-X710 all-in-One fluorescence microscope and a Nikon Ti2E/CSU-W1 spinning disc confocal system. Quantification of SOX9 (+) cells was performed on high resolution SOX9 IHC staining images with ImageJ. At least two sections were analyzed for each mouse. At least three mice for each genotype were analyzed.

MicroCT analysis

MicroCT analysis was performed on the tails of P60 mice and P1 mouse pups. All samples were fixed in 10% neutral-buffered formalin for 3 days at room temperature, thoroughly washed, and scanned on a Bruker SkyScan 1276 (Bruker Corporation, Billerica, Massachusetts). The tails were scanned at 50 kV and 200 µA with a 0.25 mm Al filter, with a 3 µm voxel size. The mouse pups were first proceeded for Alcian Blue/Alizarin Red skeletal stain using standard acid-alcohol conditions and cleared in 1% KOH and Glycerol. These embryos were scanned in glycerol at 50 kV and 100 µA with a 0.5 mm Al filter, with a 3 µm voxel size. 3D Rendering and analysis was done using Bruker CTVox and CTAn software.

Costal chondrocytes isolation and maturation

Murine costal chondrocytes were isolated as previously described by (67) with modifications. Briefly, anterior rib cages and sterna were isolated from 5-day-old wild-type, *Sox9*$^{del/+}$ and *Sox9*$^{del/del}$ pups with the soft tissue removed. Rib cages were digested in 2mg/ml Pronase (Roche) solution at 37°C for 1 hour with constant agitation, followed by 1-hour digestion in 3mg/ml collagenase D (Roche) solution in high-glucose Dulbecco's modified Eagle's medium (DMEM, Gibco) at 37°C. The rib cages were then transferred into a petri dish and digested in collagenase D (3 mg/ml in high-glucose DMEM) for 4 to 6 hours. Murine costal chondrocyte

cell suspensions were filtered through 40µm filters and seeded at a density of 200,000 cells per well in 24-well tissue culture plates. Cells were maturated with maturation medium [highglucose DMEM supplemented with 10% fetal bovine serum, 1% penicillin/streptomycin, and 50µg/ml ascorbic acid (Sigma, A4403)] for 10 days with changing of the medium in every two days. After 10 days of maturation, cells were fixed with 500µl of 10% Formaldehyde at RT for 20min, thoroughly washed with PBS, and incubated with Alcian Blue staining solution (Sigma, B8438) or anti-SOX9 antibody (EMD Millipore AB5535, 1:400) overnight at room temperature or 4°C. The next day Alcian Blue stained cells were washed with deionized water and air-dried overnight. The SOX9 antibody-stained cells were developed with a secondary antibody Alexa Flour 488 Goat anti Rabbit (A11034, 1:1500).

RNA isolation and real-time RT-PCR

RNA was isolated from primary costal chondrocytes without maturation with a QIAGEN RNeasy mini kit (QIAGEN 74104). Reverse transcription was performed using 500 ng total RNA with an iScript cDNA synthesis kit (Bio-Rad 1708840). Real-time RT-PCR (qPCR) analyses were performed as previously described by (67). Gene expression was normalized to b-actin mRNA and relative expression was calculated using the 2-(ΔΔCt) method. The mouse-specific primers were used to quantify gene expression (Supplemental Table 1). Real-time RT-PCR efficiency was optimized and melting curve analyses of products were performed to ensure reaction specificity.

Protein extraction and western blot of the primary cells

Total proteins were extracted from primary costal chondrocytes without maturation with protein extraction buffer [50mM HEPES, 1.5mM EDTA (pH 8.0), 150mM NaCl, 10% glycerol, 1% Triton X-100] supplemented with protease and phosphatase inhibitors (Roche). 10mg of protein from each sample was resolved by 4–15% SDS-polyacrylamide gel

electrophoresis and transferred to the nitrocellulose membranes. Western blots were then blocked with LI-COR blocking buffer and incubated overnight with primary antibodies anti-SOX9 (EMD Millipore AB5535, 1:1000) and anti-GAPDH (Cell Signaling, #2118, 1:2500) at 4˚C with gentle rocking. The next day western blots were detected with the LI-COR Odyssey infrared imaging system. Quantification of band intensity was conducted with ImageJ. Three independent experiments were performed with reproducible results.

RNA-sequencing and data analysis

RNA-sequencing was performed on costal chondrocytes isolated from P5 *Sox9*$^{del/+}$ mice and *Sox9*$^{del/del}$ mice. Briefly, anterior rib cages and sterna were isolated from P5 pups, digested in 2mg/ml Pronase solution at 37°C for 1 hour with constant agitation, followed by 1-hour digestion in 3mg/ml collagenase D solution in 1XPBS. Cells were disassociated, thoroughly washed in 1XPBS and filtered through a 40μm cell strainer. Cells were pelleted by centrifuging at 300 × g for 4 min at room temperature. RNA was isolated with a QIAGEN RNeasy mini kit (QIAGEN 74104).

Library preparation, RNA sequencing, and bioinformatics analysis were performed by Novogene Co., Ltd. Messenger RNA was purified from total RNA using poly-T oligo-attached magnetic beads. After fragmentation, the first strand of cDNA was synthesized using random hexamer primers, followed by the second strand of cDNA synthesis. The library was examined with Qubit and real-time PCR for quantification and a bioanalyzer for size distribution detection. Quantified libraries were pooled and sequenced on Illumina platforms and pairedend reads were generated. Raw data in fastq format were firstly processed through in-house Perl scripts and clean reads were obtained. Reference genome and gene model annotation files were downloaded from the genome website directly. Index of the reference genome was built using Hisat2 v2.0.5 and paired-end clean reads were aligned to the reference genome using Hisat2

v2.0.5. featureCounts v1.5.0-p3 was used to count the reads numbers mapped to each gene. FPKM of each gene was calculated based on the length of the gene and the reads count mapped to this gene. Differential expression analysis was performed using the DESeq2 R package (1.20.0). The resulting P-values were adjusted using Benjamini and Hochberg's approach for controlling the false discovery rate. Genes with an adjusted P-value <=0.05 found by DESeq2 were assigned as differentially expressed. Gene Ontology (GO) enrichment analysis of differentially expressed genes was implemented by the clusterProfiler R package, in which gene length bias was corrected. GO terms with corrected P value less than 0.05 were considered significantly enriched in differential expressed genes.

Statistics

Statistical analyses were performed in GraphPad Prism 9.1.2 (GraphPad Software Inc, SanDiego, CA) or SPSS version 15.0 (SPSS). For luciferase assay, half-life analysis, Cobb angle, and gene expression analysis to compare two or more experimental groups, 2-tailed Student's t-test and Welch one-way ANOVA followed by Turkey's multiple comparison test were applied when appropriate. A p-value of less than 0.05 is considered statistically significant.

Study approval

This study was approved by the Institutional Review Board of Peking Union Medical College Hospital (JS-2364). Written informed consent was obtained from each patient or legal guardian of the patient. All mouse studies and procedures were approved by the Animal Studies Committee at the University of Texas at Austin.

968 **Statement**

969 The patient ID is a unique research identifier that cannot be linked back to the original patients
970 outside of the research group. Medical history details have also been removed to protect the
971 patients' privacy.

972

973 **Data availability**

974 Data are available from the corresponding author upon reasonable request.

975 ## Author contributions

976 N.W., R.S.G., L.W., Z.L. and S.Z. conceptualized the project. L.W., Z.L., S.Z. L.Z., Xiaoxin.L.,
977 N.W. and R.S.G. designed the study. L.W., S.Z., Z.L., C.Q., B.T., G.H., R.S.G. L.L. Xinyu.L.
978 and L.Z. performed the experiments. S.Z., L.W., Z.L., K.X., C.M.K, Xiaoxin.L., R.S.G., H.G.
979 and L.L. validated the data. N.W., S.Z., L.W., Z.L., H.G., S.Y., V.A., S.M., S.W., Y.N., R.S.G.
980 and T.J.Z. analyzed the data. L.W., S.Z., Z.L., K.X., N.W. and R.S.G. wrote the manuscript.
981 S.Z., Z.L., L.W., K.X., N.W., Z.W., C.Q., Xinyu.L. and R.S.G. critically revised the
982 manuscript. Z.L., R.S.G., N.W. and Z.W. supervised the work. All authors have read and
983 approved the final submitted manuscript. The first authorship is shared by Z.L., L.W., S.Z., and
984 K.X. The order was determined based on their respective contributions and efforts to the study.

985

986 **Acknowledgments**

987 We thank Dr. Yunjia Wang at the Department of Spine and Orthopaedics in Xiangya
988 Hospital/Central South University, and Ms. Karagan Day at the Department of Pediatrics in
989 Dell Medical School of the University of Texas at Austin for their supporting work in mouse

990 husbandry and X-ray image taking. We also thank Nanjing Geneseeq Technology Inc. for the
991 technical help in sequencing and Ekitech Technology Inc. for the technical support in database
992 and data management.

993

Funding

This research was funded in part by the National Natural Science Foundation of China (81930068 to Z.W., 2102522 to L.W., 82072391 to N.W., 881972037 and 82172382 to J.Z., and 81874022 and 82172483 to X.L.), Beijing Natural Science Foundation (JQ20032 to N.W.), CAMS Innovation Fund for Medical Sciences (CIFMS, 2021-I2M-1-051 to J.Z. and N.W., 2021-I2M-1-052 to Z.W., 2020-I2M-C&T-B-030 to J.Z.), National High Level Hospital Clinical Research Funding (2022-PUMCH-D-007 to J.Z. and N.W., 2022-PUMCH-C-033 to N.W.), National Institute of Arthritis and Musculoskeletal and Skin Diseases of the National Institutes of Health under Award (R01AR072009 to R.S.G., K99AR077090 to Z.L.), Shandong Natural Science Foundation (ZR202102210113 to L.W.), and the Non-profit Central Research Institute Fund of Chinese Academy of Medical Sciences (No. 2019PT320025 to N.W.).

SUPPLEMENTAL FIGURE LEGENDS

Supplemental Figure 1. The 3D structures of SOX9 are predicted by AlphaFold. (**A**) A model of human SOX9 was built by AlphaFold (htts://alphafold.ebi.ac.uk/). (**B**) Ile73 is predicted to be important for stabilizing alpha-helical interactions. (**C**) Met113 is predicted to stabilize alpha-helical interactions through a single hydrogen bond with Gln117 and two hydrogen bonds with Aan110. (**D**) Ala133 is predicted to stabilize alpha-helical interactions by a hydrogen bond with Ser136. (**E**) Gly276 is predicted to hydrogen bond with Asp274. Asp272 is also predicted to hydrogen bond with Asp274 by stabilizing an alpha-helical structure.

Supplemental Figure 2. Equal amounts of SOX9 proteins were used for the EMSA assay. **(A)** Western blotting of anti-GFP was performed on total protein extracted from blank Cos-7 cells (Blank), Cos-7 cells transfected with empty EGFP expression vectors (Control), wild-type SOX9 (WT), or Ile73Thr, Met113Leu, and Ala133Gly SOX9 variants that were cloned into the EGFP expression vectors at 48 hours post-transfection. GAPDH is used as a loading control. No obvious changes in expression were observed among wild-type and variant SOX9 proteins. (**B**) Quantification analysis shows that comparable amounts of SOX9 were detected among wild-type and various SOX9 variant proteins. Bars are plotted with mean and SD. Each dot represents one experiment analyzed. The statistical difference is evaluated by one-way ANOVA followed by Tukey's multiple comparison test. ns: not significant. (n=3 experiments.)

Supplemental Figure 3. Optimization of the luciferase assay. (A) Western blotting was performed on total protein extracted from blank Cos-7 cells (Blank), Cos-7 cells transfected with wild-type SOX9 construct (Wild type), or Ile73Thr, Gly276Cys, Met113Leu, Ala133Gly, and Asp276Del SOX9 variants at 48 hours post-transfection. GAPDH is used as a loading

control. No obvious changes in expression were observed among wild-type and variant SOX9 proteins. **(B)** Quantification analysis shows that comparable amounts of SOX9 were detected among wild-type and various SOX9 variant proteins. Bars are plotted with mean and SD. Each dot represents one experiment analyzed. The statistical difference is evaluated by one-way ANOVA followed by Tukey's multiple comparison test. ns: not significant. (n=3 experiments.) **(C)** A standard curve was generated to optimize the transfection dose for the luciferase assays. SOX9-expression plasmids were diluted to a gradient of concentration with the final amount from 10^{-4} to 10^{6} ng. Relative luciferase activity was normalized to the Renilla internal control. The linear range of the SOX9-mediated reporter transactivation is between 1ng-100ng. 50ng of SOX9-expression plasmids was selected for luciferase assays shown in Figure 2B. n=3 experiments.

Supplemental Figure 4. Expression of extracellular matrix components in P5 mouse tail sections. (A-B'') Representative Alcian Blue Hematoxylin /Orange G (ABH/OG) staining (**AA''**) and IHC staining of SOX9 (**B-B''**) on unwedged IVD in tail sections of P5 Sox9del/del mutant mice. The endplate is indicated with a dot line and a vertical bar in (**A'**) and (**B'**). The boundary between inner and outer annulus fibrosus is indicated with a dot-line in (**A''**) and (**B''**). (n=3.) C-H, IHC analysis of COLII **(C-E)** and COLX **(F-H)** on tail sections of P5 wildtype, $Sox9^{del/+}$, and $Sox9^{del/del}$ mice. n=3 for each genotype. Scale bars: 100μm. EP: endplate; GP-p: proliferative growth plate; GP-h: hypertrophic growth plate; AF-i: inner annulus fibrosus; AF-o: outer annulus fibrosus.

Supplemental Figure 5. Assessment of skeletal development in *Sox9* loss of function mutant mice. (**A-C**) Representative skeletal preps of Cre(-) wild-type (**A**), heterozygous *Col2a1-Cre;* $Sox9^{flox/+}$ mutant (**B**), and compound heterozygous *Col2a1-Cre;* $Sox9^{flox/del}$ mutant

mice (**C**) at P1. **(D-F)** Representative MicroCT images of Cre(-) wild-type (**D**), heterozygous *Col2a1-Cre; Sox9$^{flox/+}$* mutant (**E**), and compound heterozygous *Col2a1-Cre; Sox9$^{flox/del}$* mutant mice (**F**) at P1. n=4 for each genotype. Scale bar: 1mm.

Supplemental Figure 6. Young adult *Sox9$^{del/del}$* mice display mild rib cage deformities.

(**A-C**) Representative sagittal X-ray images of wild-type (**A**), *Sox9$^{del/+}$* (**B**), and *Sox9$^{del/del}$* mice (**C**) at P60. Red arrows indicate the curvature of the distal ribs (**C**). n=4 for wild-type mice; 2 males, 2 females. n=8 for *Sox9$^{del/+}$* mice; 5 males, 3 females. n=7 for *Sox9$^{del/del}$* mice; 4 males, 3 females. Scale bar: 10mm.

Supplemental Figure 7. Mature adult *Sox9$^{del/del}$* mice display rib cage deformities and impaired ossification in the endplate of the intervertebral discs. (**A-E**) Additional sagittal X-ray images of wild-type (**A**), *Sox9$^{del/+}$* (**B**), and *Sox9$^{del/del}$* mice (**C-E**) at 6 months. Red arrows indicate the bending of the sternums (**B-D**) or the curvature of the distal ribs I. (**F-J'**) Additional ABH/OG staining of lumbar IVDs (L3/4 or L4/5) of wild-type (**F, F'**), *Sox9$^{del/+}$* (**G, G'**) and *Sox9$^{del/del}$* (**H-J'**) mice at 6 months. Wild-type and *Sox9$^{del/+}$* mice consistently showed ossification within the endplate at 6 months (yellow arrows, **F'** and **G'**). On the contrary, *Sox9$^{del/del}$* mice showed reduced endplate ossification (yellow arrow, **J'**) or persistency of hypertrophic chondrocyte-like cells within the endplate (yellow asterisks, **H'**, **I'**). n=3 for each genotype. Scale bars: 10mm in **A**; 100μm in **F-F'**. AF: annulus fibrosus; EP: endplate; GP: growth plate; NP: nucleus pulposus.

Supplemental Figure 8. SOX9 protein expression in costal chondrocytes. (**A**) Representative Western blot image of SOX9 performed on P5 costal chondrocytes isolated

from three different genotypes of mice. GAPDH is used as a loading control (n=3 experiments). (**B**) Quantification analysis shows that comparable amounts of SOX9 protein were detected among three genotypes. Bars are plotted with mean and 95%CI. Each dot represents one experiment analyzed. The statistical difference is evaluated by one-way ANOVA followed by Tukey's multiple comparison test. ns: not significant (n=3 experiments).

Supplemental Table 1. Primers used for amplification of the DNA segments containing the candidate *SOX9* variants and for RT-PCR quantification.

Supplemental Table 2. Sequences of the SOX9 binding motifs used for EMSA and luciferase assay.

Supplemental Table 3. Differential gene expression analysis of primary costal chondrocytes derived from $Sox9^{del/+}$ and $Sox9^{del/del}$ mutant mice.

Supplemental Table 4. GO-terms associated with differential gene expression analysis of primary costal chondrocytes derived from $Sox9^{del/+}$ and $Sox9^{del/del}$ mutant mice.

1095 **Table 1.** Clinical and genetic features of the four probands

ID	**RDD2003P0397**	**SCO2003P0412**	**SCO2003P0060**	**SCO2003P1898**
Variant information				
HGVS	c.337A>C (p.Met113Leu)	c.398C>G (p.Ala133Gly)	c.218T>C (p.Ile73Thr)	c.826G>T (p.Gly276Cys)
Origin	*de novo*	Unknown	*de novo*	*de novo*
Domain	HMG	HMG	DIM	TAM
CADD	27.3	26.5	24.1	29.6
Skeleton, joints and limbs				
Scoliosis	-	+	+	+
Kyphosis	+	-	+	-
Lordosis	+	-	-	-
Vertebral malformation	Fusion of cervical vertebrae	L2 wedged vertebra	T6 wedged vertebra	Fusion of thoracic vertebrae
Other skeletal deformity	Hypoplastic scapulae	Brachydactyly	Hypoplastic scapulae, Short stature	Spinal bifida occulta, Clinodactyly

1096

Abbreviations: DIM: dimerization domain; HMG: high mobility group domain; TAM: transactivation middle domain.

REFERENCES

1. Lefebvre V. Roles and regulation of SOX transcription factors in skeletogenesis. *Curr Top Dev Biol.* 2019;133:171-93.
2. Lefebvre V, and Dvir-Ginzberg M. SOX9 and the many facets of its regulation in the chondrocyte lineage. *Connect Tissue Res.* 2017;58(1):2-14.
3. Akiyama H, Chaboissier MC, Martin JF, Schedl A, and de Crombrugghe B. The transcription factor Sox9 has essential roles in successive steps of the chondrocyte differentiation pathway and is required for expression of Sox5 and Sox6. *Genes Dev.* 2002;16(21):2813-28.
4. Barrionuevo F, Taketo MM, Scherer G, and Kispert A. Sox9 is required for notochord maintenance in mice. *Dev Biol.* 2006;295(1):128-40.
5. Sugimoto Y, Takimoto A, Akiyama H, Kist R, Scherer G, Nakamura T, et al. Scx+/Sox9+ progenitors contribute to the establishment of the junction between cartilage and tendon/ligament. *Development.* 2013;140(11):2280-8.
6. Henry SP, Liang S, Akdemir KC, and de Crombrugghe B. The postnatal role of Sox9 in cartilage. *J Bone Miner Res.* 2012;27(12):2511-25.
7. Tsingas M, Ottone OK, Haseeb A, Barve RA, Shapiro IM, Lefebvre V, et al. Sox9 deletion causes severe intervertebral disc degeneration characterized by apoptosis, matrix remodeling, and compartment-specific transcriptomic changes. *Matrix Biol.* 2020;94:110-33.
8. Haseeb A, and Lefebvre V. The SOXE transcription factors-SOX8, SOX9 and SOX10-share a bi-partite transactivation mechanism. *Nucleic Acids Res.* 2019;47(13):6917-31.
9. Oh CD, Maity SN, Lu JF, Zhang J, Liang S, Coustry F, et al. Identification of SOX9 interaction sites in the genome of chondrocytes. *PLoS One.* 2010;5(4):e10113.

10. Barrionuevo F, and Scherer G. SOX E genes: SOX9 and SOX8 in mammalian testis development. *Int J Biochem Cell Biol.* 2010;42(3):433-6.

11. Zhao L, Li G, and Zhou GQ. SOX9 directly binds CREB as a novel synergism with the PKA pathway in BMP-2-induced osteochondrogenic differentiation. *J Bone Miner Res.* 2009;24(5):826-36.

12. Miyake A, Kou I, Takahashi Y, Johnson TA, Ogura Y, Dai J, et al. Identification of a susceptibility locus for severe adolescent idiopathic scoliosis on chromosome 17q24.3. *PLoS One.* 2013;8(9):e72802.

13. Takeda K, Kou I, Otomo N, Grauers A, Fan YH, Ogura Y, et al. A multiethnic meta-analysis defined the association of rs12946942 with severe adolescent idiopathic scoliosis. *J Hum Genet.* 2019;64(5):493-8.

14. Wagner T, Wirth J, Meyer J, Zabel B, Held M, Zimmer J, et al. Autosomal sex reversal and campomelic dysplasia are caused by mutations in and around the SRY-related gene SOX9. *Cell.* 1994;79(6):1111-20.

15. Foster JW, Dominguez-Steglich MA, Guioli S, Kwok C, Weller PA, Stevanovic M, et al. Campomelic dysplasia and autosomal sex reversal caused by mutations in an SRY-related gene. *Nature.* 1994;372(6506):525-30.

16. Houston CS, Opitz JM, Spranger JW, Macpherson RI, Reed MH, Gilbert EF, et al. The campomelic syndrome: review, report of 17 cases, and follow-up on the currently 17-year-old boy first reported by Maroteaux et al in 1971. *Am J Med Genet.* 1983;15(1):3-28.

17. Bernard P, Tang P, Liu S, Dewing P, Harley VR, and Vilain E. Dimerization of SOX9 is required for chondrogenesis, but not for sex determination. *Hum Mol Genet.* 2003;12(14):1755-65.

1148 18. Lewandoski M, Meyers EN, and Martin GR. Analysis of Fgf8 gene function in
1149 vertebrate development. *Cold Spring Harb Symp Quant Biol.* 1997;62:159-68.
1150 19. Sock E, Pagon RA, Keymolen K, Lissens W, Wegner M, and Scherer G. Loss of DNA-
1151 dependent dimerization of the transcription factor SOX9 as a cause for campomelic
1152 dysplasia. *Hum Mol Genet.* 2003;12(12):1439-47.
1153 20. Leipoldt M, Erdel M, Bien-Willner GA, Smyk M, Theurl M, Yatsenko SA, et al. Two
1154 novel translocation breakpoints upstream of SOX9 define borders of the proximal and
1155 distal breakpoint cluster region in campomelic dysplasia. *Clin Genet.* 2007;71(1):67-
1156 75.
1157 21. Velagaleti GV, Bien-Willner GA, Northup JK, Lockhart LH, Hawkins JC, Jalal SM, et
1158 al. Position effects due to chromosome breakpoints that map approximately 900 Kb
1159 upstream and approximately 1.3 Mb downstream of SOX9 in two patients with
1160 campomelic dysplasia. *Am J Hum Genet.* 2005;76(4):652-62.
1161 22. Pfeifer D, Kist R, Dewar K, Devon K, Lander ES, Birren B, et al. Campomelic
1162 dysplasia translocation breakpoints are scattered over 1 Mb proximal to SOX9:
1163 evidence for an extended control region. *Am J Hum Genet.* 1999;65(1):111-24.
1164 23. Bi W, Huang W, Whitworth DJ, Deng JM, Zhang Z, Behringer RR, et al.
1165 Haploinsufficiency of Sox9 results in defective cartilage primordia and premature
1166 skeletal mineralization. *Proc Natl Acad Sci U S A.* 2001;98(12):6698-703.
1167 24. Au TYK, Yip RKH, Wynn SL, Tan TY, Fu A, Geng YH, et al. Hypomorphic and
1168 dominant-negative impact of truncated SOX9 dysregulates Hedgehog-Wnt signaling,
1169 causing campomelia. *Proc Natl Acad Sci U S A.* 2023;120(1):e2208623119.
1170 25. Macpherson RI, Skinner SA, and Donnenfeld AE. Acampomelic campomelic
1171 dysplasia. *Pediatr Radiol.* 1989;20(1-2):90-3.

1172 26. von Bohlen AE, Bohm J, Pop R, Johnson DS, Tolmie J, Stucker R, et al. A mutation
1173 creating an upstream initiation codon in the SOX9 5' UTR causes acampomelic
1174 campomelic dysplasia. *Mol Genet Genomic Med.* 2017;5(3):261-8.
1175 27. Vivekanandan S, Moovarkumudalvan B, Lescar J, and Kolatkar PR. Crystallization and
1176 X-ray diffraction analysis of the HMG domain of the chondrogenesis master regulator
1177 Sox9 in complex with a ChIP-Seq-identified DNA element. *Acta Crystallogr F Struct*
1178 *Biol Commun.* 2015;71(Pt 11):1437-41.
1179 28. Bell DM, Leung KK, Wheatley SC, Ng LJ, Zhou S, Ling KW, et al. SOX9 directly
1180 regulates the type-II collagen gene. *Nat Genet.* 1997;16(2):174-8.
1181 29. Lefebvre V, Zhou G, Mukhopadhyay K, Smith CN, Zhang Z, Eberspaecher H, et al.
1182 An 18-base-pair sequence in the mouse proalpha1(II) collagen gene is sufficient for
1183 expression in cartilage and binds nuclear proteins that are selectively expressed in
1184 chondrocytes. *Mol Cell Biol.* 1996;16(8):4512-23.
1185 30. Bridgewater LC, Lefebvre V, and de Crombrugghe B. Chondrocyte-specific enhancer
1186 elements in the Col11a2 gene resemble the Col2a1 tissue-specific enhancer. *J Biol*
1187 *Chem.* 1998;273(24):14998-5006.
1188 31. McDowall S, Argentaro A, Ranganathan S, Weller P, Mertin S, Mansour S, et al.
1189 Functional and structural studies of wild type SOX9 and mutations causing campomelic
1190 dysplasia. *J Biol Chem.* 1999;274(34):24023-30.
1191 32. Csukasi F, Duran I, Zhang W, Martin JH, Barad M, Bamshad M, et al. Dominant-
1192 negative SOX9 mutations in campomelic dysplasia. *Hum Mutat.* 2019;40(12):2344-52.
1193 33. Schock EN, and LaBonne C. Sorting Sox: Diverse Roles for Sox Transcription Factors
1194 During Neural Crest and Craniofacial Development. *Front Physiol.* 2020;11:606889.
1195 34. Unger S, Scherer G, and Superti-Furga A. In: Adam MP, Everman DB, Mirzaa GM,
1196 Pagon RA, Wallace SE, Bean LJH, et al. eds. *GeneReviews((R))*. Seattle (WA); 1993.

35. Wu N, Wang L, Hu J, Zhao S, Liu B, Li Y, et al. A Recurrent Rare SOX9 Variant (M469V) is Associated with Congenital Vertebral Malformations. *Curr Gene Ther.* 2019;19(4):242-7.

36. Calvache CA, Vasquez EC, Romero VI, Hosomichi K, and Pozo JC. Novel SRY-box transcription factor 9 variant in campomelic dysplasia and the location of missense and nonsense variants along the protein domains: A case report. *Front Pediatr.* 2022;10:975947.

37. Geraldo MT, Valente GT, Nakajima RT, and Martins C. Dimerization and Transactivation Domains as Candidates for Functional Modulation and Diversity of Sox9. *PLoS One.* 2016;11(5):e0156199.

38. Staffler A, Hammel M, Wahlbuhl M, Bidlingmaier C, Flemmer AW, Pagel P, et al. Heterozygous SOX9 mutations allowing for residual DNA-binding and transcriptional activation lead to the acampomelic variant of campomelic dysplasia. *Hum Mutat.* 2010;31(6):E1436-44.

39. Wada Y, Nishimura G, Nagai T, Sawai H, Yoshikata M, Miyagawa S, et al. Mutation analysis of SOX9 and single copy number variant analysis of the upstream region in eight patients with campomelic dysplasia and acampomelic campomelic dysplasia. *Am J Med Genet A.* 2009;149A(12):2882-5.

40. Retterer K, Juusola J, Cho MT, Vitazka P, Millan F, Gibellini F, et al. Clinical application of whole-exome sequencing across clinical indications. *Genet Med.* 2016;18(7):696-704.

41. Richards S, Aziz N, Bale S, Bick D, Das S, Gastier-Foster J, et al. Standards and guidelines for the interpretation of sequence variants: a joint consensus recommendation of the American College of Medical Genetics and Genomics and the Association for Molecular Pathology. *Genet Med.* 2015;17(5):405-24.

1222 42. Jumper J, Evans R, Pritzel A, Green T, Figurnov M, Ronneberger O, et al. Highly
1223 accurate protein structure prediction with AlphaFold. *Nature.* 2021;596(7873):583-9.
1224 43. Huang YH, Jankowski A, Cheah KS, Prabhakar S, and Jauch R. SOXE transcription
1225 factors form selective dimers on non-compact DNA motifs through multifaceted
1226 interactions between dimerization and high-mobility group domains. *Sci Rep.*
1227 2015;5:10398.
1228 44. Bridgewater LC, Walker MD, Miller GC, Ellison TA, Holsinger LD, Potter JL, et al.
1229 Adjacent DNA sequences modulate Sox9 transcriptional activation at paired Sox sites
1230 in three chondrocyte-specific enhancer elements. *Nucleic Acids Res.* 2003;31(5):1541-
1231 53.
1232 45. Giampietro PF, Raggio CL, Blank RD, McCarty C, Broeckel U, and Pickart MA.
1233 Clinical, genetic and environmental factors associated with congenital vertebral
1234 malformations. *Mol Syndromol.* 2013;4(1-2):94-105.
1235 46. Cobb JR. Scoliosis; quo vadis. *J Bone Joint Surg Am.* 1958;40-A(3):507-10.
1236 47. Abid I, Ewais MM, Marranca J, and Jaroszewski DE. Pectus Excavatum: A Review of
1237 Diagnosis and Current Treatment Options. *J Am Osteopath Assoc.* 2017;117(2):106-
1238 13.
1239 48. David VL. Current Concepts in the Etiology and Pathogenesis of Pectus Excavatum in
1240 Humans-A Systematic Review. *J Clin Med.* 2022;11(5).
1241 49. Haseeb A, Kc R, Angelozzi M, de Charleroy C, Rux D, Tower RJ, et al. SOX9 keeps
1242 growth plates and articular cartilage healthy by inhibiting chondrocyte
1243 dedifferentiation/osteoblastic redifferentiation. *Proc Natl Acad Sci U S A.* 2021;118(8).
1244 50. Smith LJ, Nerurkar NL, Choi KS, Harfe BD, and Elliott DM. Degeneration and
1245 regeneration of the intervertebral disc: lessons from development. *Dis Model Mech.*
1246 2011;4(1):31-41.

1247 51. Zhao CQ, Wang LM, Jiang LS, and Dai LY. The cell biology of intervertebral disc
1248 aging and degeneration. *Ageing Res Rev.* 2007;6(3):247-61.
1249 52. Hong X, Liu W, Song R, Shah JJ, Feng X, Tsang CK, et al. SOX9 is targeted for
1250 proteasomal degradation by the E3 ligase FBW7 in response to DNA damage. *Nucleic*
1251 *Acids Res.* 2016;44(18):8855-69.
1252 53. Schneider-Poetsch T, Ju J, Eyler DE, Dang Y, Bhat S, Merrick WC, et al. Inhibition of
1253 eukaryotic translation elongation by cycloheximide and lactimidomycin. *Nat Chem*
1254 *Biol.* 2010;6(3):209-17.
1255 54. Ghosh S, Laha M, Mondal S, Sengupta S, and Kaplan DL. In vitro model of
1256 mesenchymal condensation during chondrogenic development. *Biomaterials.*
1257 2009;30(33):6530-40.
1258 55. Hu G, Codina M, and Fisher S. Multiple enhancers associated with ACAN suggest
1259 highly redundant transcriptional regulation in cartilage. *Matrix Biol.* 2012;31(6):328-
1260 37.
1261 56. Leung VY, Gao B, Leung KK, Melhado IG, Wynn SL, Au TY, et al. SOX9 governs
1262 differentiation stage-specific gene expression in growth plate chondrocytes via direct
1263 concomitant transactivation and repression. *PLoS Genet.* 2011;7(11):e1002356.
1264 57. Sekido R, and Lovell-Badge R. Sex determination involves synergistic action of SRY
1265 and SF1 on a specific Sox9 enhancer. *Nature.* 2008;453(7197):930-4.
1266 58. Taniguchi Y, Kawata M, Ho Chang S, Mori D, Okada K, Kobayashi H, et al. Regulation
1267 of Chondrocyte Survival in Mouse Articular Cartilage by p63. *Arthritis Rheumatol.*
1268 2017;69(3):598-609.
1269 59. Nishimori S, Lai F, Shiraishi M, Kobayashi T, Kozhemyakina E, Yao TP, et al. PTHrP
1270 targets HDAC4 and HDAC5 to repress chondrocyte hypertrophy. *JCI Insight.*
1271 2019;4(5).

60. Burch GH, Gong Y, Liu W, Dettman RW, Curry CJ, Smith L, et al. Tenascin-X deficiency is associated with Ehlers-Danlos syndrome. *Nat Genet.* 1997;17(1):104-8.

61. Mao JR, Taylor G, Dean WB, Wagner DR, Afzal V, Lotz JC, et al. Tenascin-X deficiency mimics Ehlers-Danlos syndrome in mice through alteration of collagen deposition. *Nat Genet.* 2002;30(4):421-5.

62. Liu Z, Easson GWD, Zhao J, Makki N, Ahituv N, Hilton MJ, et al. Dysregulation of STAT3 signaling is associated with endplate-oriented herniations of the intervertebral disc in Adgrg6 mutant mice. *PLoS Genet.* 2019;15(10):e1008096.

63. Liu Z, Hussien AA, Wang Y, Heckmann T, Gonzalez R, Karner CM, et al. An adhesion G protein-coupled receptor is required in cartilaginous and dense connective tissues to maintain spine alignment. *Elife.* 2021;10.

64. Kou I, Takahashi Y, Johnson TA, Takahashi A, Guo L, Dai J, et al. Genetic variants in GPR126 are associated with adolescent idiopathic scoliosis. *Nat Genet.* 2013;45(6):676-9.

65. Zhao S, Zhang Y, Chen W, Li W, Wang S, Wang L, et al. Diagnostic yield and clinical impact of exome sequencing in early-onset scoliosis (EOS). *J Med Genet.* 2021;58(1):41-7.

66. Chen N, Zhao S, Jolly A, Wang L, Pan H, Yuan J, et al. Perturbations of genes essential for Mullerian duct and Wolffian duct development in Mayer-Rokitansky-Kuster-Hauser syndrome. *Am J Hum Genet.* 2021;108(2):337-45.

67. Liu Z, Chen J, Mirando AJ, Wang C, Zuscik MJ, O'Keefe RJ, et al. A dual role for NOTCH signaling in joint cartilage maintenance and osteoarthritis. *Sci Signal.* 2015;8(386):ra71.